ACOUSTIC TRANSMISSION IMAGING FOR FLOW DIAGNOSTICS

Thesis by
Bernd Otto Trebitz

In Partial Fulfillment
of the Requirements for the Degree of
Doctor of Philosophy

California Institute of Technology
Pasadena, California

1982
(Submitted April 30, 1982)

ACKNOWLEDGEMENTS

The assistance of many persons has been invaluable throughout the course of this research effort and is greatly acknowledged.

The author would like to express his sincere appreciation to Professor Hans W. Liepmann as advisor for his patience and encouragement, without which this work could not have been completed.

Special thanks are extended to Professor Pierre Alais for his advice in the initial phase of this project and to Professor Hassan M. Nagib for loaning his airfoil swirl generator. Furthermore, the author is indebted to his advisory committee for their constructive criticism and many helpful discussions.

Thanks also go to the technical staff of GALCIT, especially to the aeronautics and electronics shop for their help during the construction phase of the apparatus. The author is grateful to Mrs. Jacquelyn Beard for her help with the manuscript, Mrs. Betty Wood for preparing the drawings and Mr. Harry Hamaguchi for the photographic work.

The financial assistance of the California Institute of Technology and the Air Force Office of Scientific Research which sponsored this project is gratefully acknowledged.

Last, but not least, the author would like to thank all his friends and fellow graduate students for many technical discussions as well as moral support which have contributed significantly to the completion of this work.

ABSTRACT

Wave propagation through a given flow field can be utilized to obtain information about the flow. Acoustic waves in particular offer the possibility of measuring velocity fields, because sound waves are convected with the flow, and temperature fields, because the acoustic index of refraction is a strong function of temperature. This work concentrates on situations where the first effect is dominating compared to the latter one.

A sound system capable of "illuminating" a flow field with ultrasonic waves and measuring the amplitude and phase distribution of the transmitted wave as a function of time was constructed. A large area transmitter and a linear receiving array were used as transducers. Parallel signal processing and interleaved data conversion and acquisition result in a maximum frame rate of 10 kHz.

The feasibility of measuring velocity disturbances with ultrasound was demonstrated by transmitting sound through a vortex, which was generated in a duct by an airfoil swirl generator. Assuming an exponential fit for the tangential velocity component, inner core radius and circulation can be determined directly from the phase change of the transmitted wave due to the vortex. A more accurate representation of the radial velocity profile can be found by digital reconstruction via the Abel inversion formula, which allows reconstruction of rotationally symmetric objects from line projections. Even though the flow field under investigation was steady, this is neither a restriction of the technique, nor of the apparatus. However, the repetition rate for consecutive data frames depends on the operating procedure.

TABLE OF CONTENTS

Chapter	Title	Page
	Acknowledgements	ii
	Abstract	iii
	Table of Contents	iv
	List of Figures	vi
	List of Symbols	vii
1.	INTRODUCTION	1
2.	SOUND AS A DIAGNOSTIC TOOL	3
	2.1. Imaging Techniques	3
	2.2. Measurement Quantities	4
	2.3. Depth Reconstruction via Abel Inversion	5
3.	SOUND SYSTEM	9
	3.1. Transmitter and Receiving Array	9
	3.2. Signal Processing	12
	3.3. Data Acquisition	14
4.	APPLICATION TO A SWIRLING FLOW IN A DUCT	16
	4.1. Experimental Facility	16
	4.2. Results	21
	4.2.1. Mean Flow Results	23
	4.2.2. Swirling Flow Results	26
	4.3. Digital Reconstruction of Tangential Velocity Profile	32
5.	CONCLUSION AND OUTLOOK	37
6.	References	39

Appendices

A. Receiving Array 40

B. Signal Processing Electronics 42

C. Data Acquisition Electronics 46

D. Straight Ray Integration 49

E. Plume Experiment 51

LIST OF FIGURES

Figure	Title	Page
2-1	Transmission Imaging	6
3-1	Piezoelectric Transducer Array	10
3-2	System Block Diagram	13
4-1	Experimental Facility (Top view)	17
4-2	Airfoil Swirl Generator	18
4-3	Transmitter-Receiver Assembly	20
4-4	Amplitude and Phase Distribution for U_∞=75 ft/sec and $\alpha = \pm 0°$	24
4-5	Amplitude and Phase Distribution for U_∞=75 ft/sec and $\alpha = \pm 5°$	27
4-6	Phase Signature of a Vortex Generated with U_∞=75 ft/sec and $\alpha = \pm 5°$	29
4-7	Input Phase Distribution for Abel Inversion	33
4-8	Tangential Velocity Profile	35
B-1	Phase-Sensitive Detector Circuit	43
B-2	Phase-Locked-Loop Circuit for Generating Reference Signals	45
C-1	Structure of Processing Electronics	47
E-1	Schematic of Plume Experiment	52
E-2	Acoustic Amplitude Transmission Image of Plume at 15 W	54
E-3	Temperature Distribution Through Plume at 15 W	55

LIST OF SYMBOLS

a	Speed of sound
A	Amplitude
D	Diameter
F	Focal length
k	Wavenumber
L	Distance between transmitter and receiving array
n	Index of refraction
N	Near field
r_0	Inner core radius
R	Radius of velocity disturbance
s	Array element spacing
t	Time
$\vec{u}$	Flow velocity
U_∞	Free stream velocity
v	Tangential velocity component
α	Wing angle on airfoil swirl generator
Γ	Circulation
ε	Small quantity
λ	Wavelength
φ	Phase
$\Delta\Phi$	Peak to peak phaseshift

Chapter 1

INTRODUCTION

The use of acoustic waves for visualizing objects gained importance in the 1950s, after the invention of wave front reconstruction (holography) by Gabor in 1948. However, the relative ease of generating coherent acoustic waves was offset by the lack of a suitable high resolution recording medium like film for optical radiation. Only due to recent developments in piezoceramic array technology is acoustic imaging used more extensively than before. Furthermore, arrays offer the advantage of measuring the phase of the wave front directly without requiring interference experiments as necessary in electromagnetic radiation.

So far acoustic imaging has been applied primarily to nondestructive testing of solids and to biomedical diagnostics. In these applications, objects are usually of high contrast and stationary or moving very slowly. This allows the use of either reflection imaging techniques or tomography. Flow fields, on the other hand, are in general of low contrast and unsteady, which excludes the previously mentioned techniques and calls for a single passage transmission technique.

Previous work on flow diagnostics has been carried out in water by Johnson, et al. (1976), and in air by Schmidt (1975). The first authors consider two circular transducer arrays in different planes of a circular pipe. A large number of time-of-flight data between different array elements allows one to algebraically reconstruct the flow field in the pipe. Schmidt and his group (e.g. Engler, et al. 1982) mechanically traverse a dual emitter-receiver assembly through a given flow field, utilizing time-of-flight data to obtain information about the flow. Even though the latter authors have investigated periodically changing flow fields,

both arrangements lack the capability of tracking general unsteady flows because the respective data acquisition times are too large. The present work investigates possibilities of using acoustic radiation for gas flow diagnostics with array technology that is not restricted to steady flows.

Chapter 2

SOUND AS A DIAGNOSTIC TOOL

In this chapter, general concepts of acoustical imaging techniques and their application to gas flow diagnostics are briefly described. In these applications, a transmission imaging technique sensitive to velocity and temperature changes in the flow is most suitable. The transmitted wave contains integrated information of the flow field, and the use of digital reconstruction techniques is required to obtain depth information.

2.1. Imaging Techniques

Imaging techniques can be classified into two groups: reflection and transmission imaging techniques. In both cases, a uniform beam illuminates an object and is partially reflected and partially transmitted, depending on the object properties. Both parts contain information about the object, and the name of the imaging technique is derived from the part that is considered as carrier of information. This part is also called the object beam and is recorded on a suitable recording medium.

This work is concerned with objects that are flow fields, where transmission coefficients are generally much larger than reflection coefficients. Even though the reflected beam consists of scattered information alone, it is generally too weak to be picked up. Therefore, most promising for flow diagnostics is a transmission imaging technique.

2.2. Measurement Quantities

The object beam contains information about the flow field which depends on the type of illumination. For optical illumination, one obtains pictures which are proportional to density or derivatives of density, because the optical index of refraction describing the object is predominantly a function of density. Illuminating a flow field with sound (also known as insonifying a flow field) allows one to measure flow properties which alter the acoustical index of refraction

$$n = \frac{a_0}{a} , \tag{2-1}$$

where a_0 is the undisturbed speed of sound. For a perfect gas, the sound speed, a, is a function of temperature and flow velocity, the latter one due to the convection of the sound wave with the local velocity field. Hence, acoustical imaging techniques offer the possibility of measuring temperatures and velocities in a gas flow.

In general, the object beam contains information on both temperature and velocity changes. Great care has to be taken to keep one of the effects small compared to the other one. The feasibility of measuring temperatures is demonstrated by transmitting ultrasound of 3 MHz through a temperature-driven axisymmetric plume in water (see Appendix E). However, this work concentrates on situations where the change in sound speed due to velocities is dominant compared to temperatures. Then, for flow velocities, u, small compared to a_0, the index of refraction can be written as

$$n = 1 - \frac{u}{a_0}. \tag{2-2}$$

Even though a light wave is also convected with the flow, the change in index of

refraction for light in air is nine orders of magnitude smaller than that for a sound wave. This large difference is not only due to the much larger propagation speed of light, but also to the fact that light is only partially convected with the flow.

2.3. Depth Reconstruction via Abel Inversion

The principle of transmission imaging is briefly reviewed in Figure 2-1. A plane wave illuminates an object which can be thought of as a region of nonuniform index of refraction, $n(\vec{r},t)$, given by Equation (2-2), where $n=1$ outside of this region. Amplitude and phase of the transmitted wave are detected in a plane behind the object. Since the propagating wave integrates along its path, the use of digital reconstruction techniques is required to recover depth information. Under certain assumptions one such technique leads to the well-known Abel inversion.

The most restrictive assumption in applying the Abel inversion for depth reconstruction is that the object has to be rotationally symmetric. Furthermore, it is assumed that the wave propagates along rays which remain straight throughout the entire object. In other words, ray deflections have to remain small which implies that amplitude changes can be neglected as long as neighbouring rays do not come to a focus. The phase change $\Delta\varphi$ due to a velocity field $\vec{u}(\vec{r})$ is then given by

$$\Delta\varphi(y) = -\frac{k_0}{a_0}\int_{\text{ray}} u_x(\vec{r})\,dx, \tag{2-3}$$

where k_0 is the undisturbed wave number. The wave propagates in the positive x-direction and $u_x(\vec{r})$ is the x-component of $\vec{u}(\vec{r})$, where a possible time

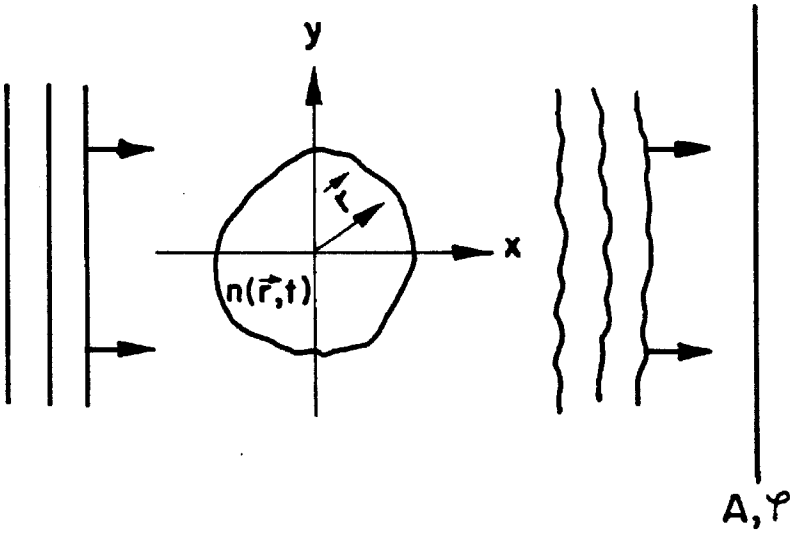

Figure 2-1. Transmission Imaging

dependence has been omitted. If the velocity field is rotationally symmetric with zero radial velocity component, then $u_x(\vec{r}) = v(r)\frac{y}{r}$, where v is the tangential velocity component and $r = |\vec{r}|$. Substitution into Equation (2-3) leads to

$$\frac{\Delta\varphi(y)}{y} = -\frac{k_0}{a_0}\int_{\text{ray}} \frac{v(r)}{r}dx \ . \tag{2-4}$$

After changing the integration variable to $r=\sqrt{x^2+y^2}$ one obtains

$$\frac{\Delta\varphi(y)}{y} = -\frac{k_0}{a_0}\int_{y^2}^{R^2}\left[\frac{v(r)}{r}\right]\frac{dr^2}{\sqrt{r^2-y^2}}, \tag{2-5}$$

where $\Delta\varphi(y)=0$ for $y \geq R$. Solving Equation (2-5) is analogous to solving Abel's equation and the result is

$$\frac{v(r)}{r} = \frac{a_0}{\pi k_0}\int_{r^2}^{R^2}\frac{d}{dy^2}\left[\frac{\Delta\varphi(y)}{y}\right]\frac{dy^2}{\sqrt{y^2-r^2}} \tag{2-6}$$

(Solomon, 1953; Gooderum & Wood, 1950). In this analysis R is the radius of the velocity disturbance which need not be finite.

The Abel inversion was successfully applied to reconstruct density fields from optical fringe shift data (e.g., Solomon, 1953). The characteristic difference in reconstructing velocity fields lies in the $\frac{1}{y}$ weighting of the acoustical phase shift, $\Delta\varphi$, which results in a velocity, $v(r)$, which is weighted by $\frac{1}{r}$. In other words, the relative importance of phase information near the centerline is much greater than that near the outer edge of the disturbance. However, this is only true for reconstructing the center region. As can be seen from the integration

limits in Equation (2-6), the reconstructed velocity, $v(r)$, depends only on phase data in the range $r < y < R$. Complete knowledge of the phase distribution is necessary in order to obtain a good reconstruction of the entire flow field.

Reconstruction techniques of the next higher level include diffraction effects, and therefore not only phase but also amplitude changes of the transmitted wave are taken into account. In this case one can abandon the restriction of rotationally symmetric objects. However, the continuous nature of the scattering flow field causes problems in the inversion process which have not yet been resolved.

Chapter 3

SOUND SYSTEM

A sound system was constructed capable of 'illuminating" a flow field with ultrasonic waves, and measuring the amplitude and phase of the transmitted wave along a line, as described in this chapter. Parallel signal processing and interleaved data conversion and acquisition result in a maximum frame rate of 10 kHz. Further digital data processing is then carried out on a PDP 11/44 computer.

3.1. Transmitter and Receiving Array

To record the object wave, a linear transducer array, which is sensitive to the instantaneous pressure of an acoustic wave impinging on it, was constructed and is shown in Figure 3-1. The sensitive area measures 3.5 x 0.5 inch and contains 100 elements resulting in a spacing, s, of 0.035 inch. The individual elements are separated by 0.008-inch wide transverse cuts half way through a piezoceramic plate 0.027 inch thick (Gulton Industries Inc., G 1408). Every element is connected with a wire to a connector on the back side of the array, where the signals are taken out for further processing. The back side of the piezoceramic plate represents the common reference potential for all signal lines. The piezoceramic plate itself is molded with epoxy in a 7 x 2.5 x 3 inch aluminum housing. On the back, the epoxy is mixed with glass balloons to attenuate any waves excited in that region. On the front, a layer of clear epoxy protects the ceramic and provides a better acoustic impedance match between the ceramic and the working medium air. The array was designed with the help of Professor Pierre Alais, and the construction was then carried out in the

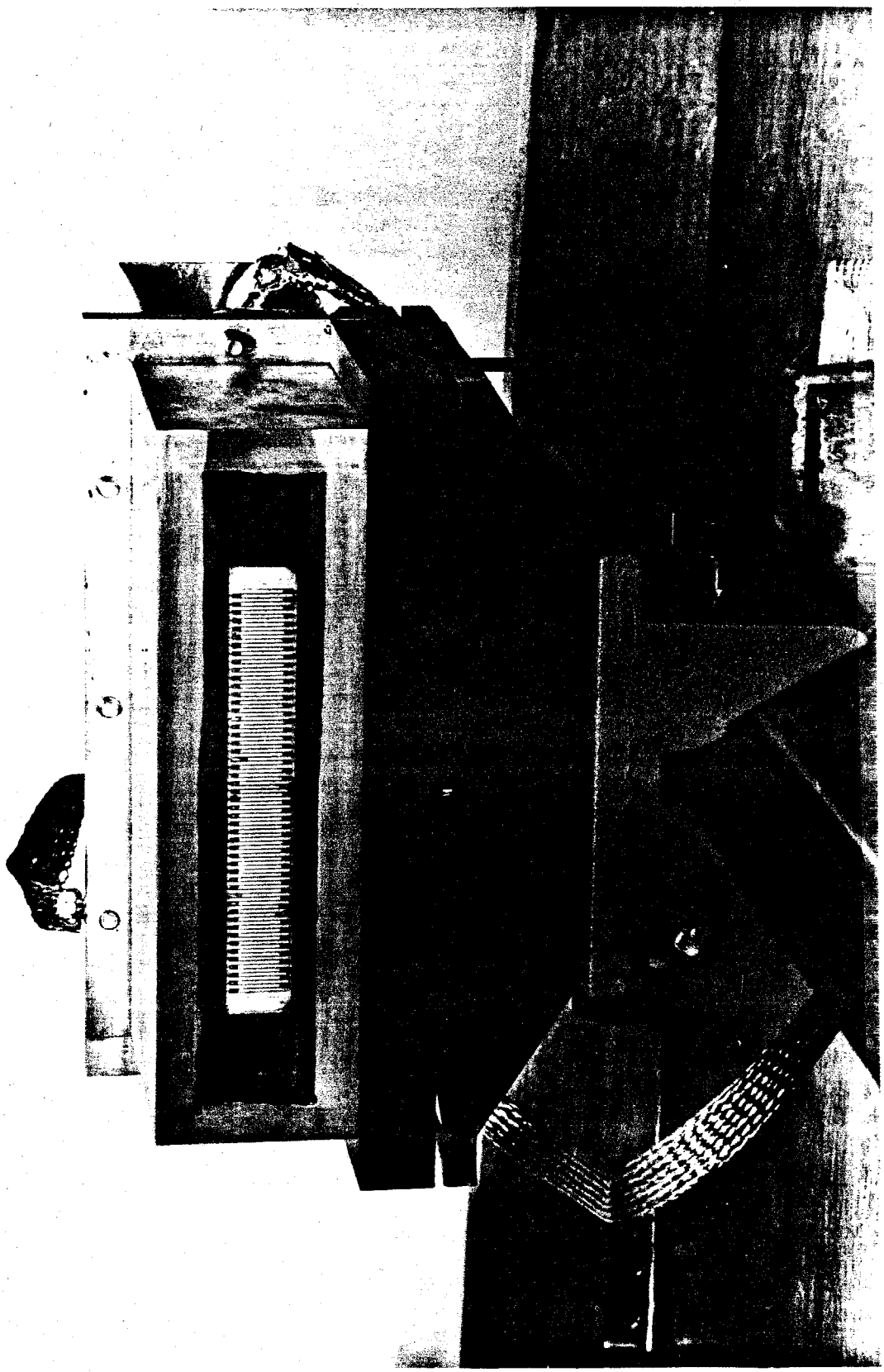

Figure 3-1. Piezoelectric Transducer Array

aeronautics shop of GALCIT (Graduate Aeronautical Laboratories of the California Institute of Technology). Further details are given in Appendix A.

The transmitter is a model 60020 transducer manufactured by Linden Laboratories, Inc. A one-inch diameter piezoelectric disc is molded in durable high-impact plastic. Even though this transducer is designed for underwater applications, it does transmit for reasonable driving levels (typically 160 Volt peak to peak) sufficient acoustic energy into the working medium air. The rated resonance frequency is 200 kHz $\pm$ 5%. However, the particular transducer used was found to give maximum output at 186 kHz, which determines the operating frequency of 186 kHz of the entire sound system. This makes the receiving array with its own resonance frequency of 3 MHz operate off resonance, resulting in a more uniform amplitude response for slight changes in frequency.

Characteristic of the transmitting beam pattern is the near field, N, defined as the length beyond which diffraction effects become important, and given by

$$N = \frac{D^2}{\lambda} \qquad (3\text{-}1)$$

(Krautkraemer, 1969), where D is the diameter of the transducer disc and λ is the wavelength. The transmitter in this sound system, radiating into air, has a near field of 87 mm. The receiving array, on the other hand, is characterized mainly by the receptivity angle, defined as the angle at which the path difference from a common source point to the edges of an array element is $\frac{\lambda}{2}$. From geometry it follows that this angle depends on the ratio $\frac{\lambda}{2s}$, where s is the array element spacing. Since $2s < \lambda$, a single array element is omnidirectional, i.e., there are no side lobes in the directivity pattern.

3.2. *Signal Processing*

The system block diagram for signal processing is shown in Figure 3-2. A function generator (Hewlett Packard, Model 651B Test Oscillator) supplies a sinusoidal signal which is amplified (Electronic Navigation Industries Inc., Model 240L RF Power Amplifier) to drive the transmitter. An analog switch between function generator and power amplifier is activated by a pulse generator (Wavetek, Model 801), in order to allow pulsed mode operation. The receiving array samples the acoustic wave along a line and passes the signals to a preamplifier and an active high-pass filter stage. This high-pass filter has a cutoff frequency of 100 kHz and blocks out all external acoustic noise that is picked up by the array. After further amplification, the resulting signals go into a phase-sensitive detector stage, whose output is proportional not only to the amplitude but also to the phase of the input signal with respect to some reference signal. To obtain amplitude *and* phase, every sensor signal is fed into *two* phase-sensitive detector circuits where the two reference signals are 90° out of phase to each other. These two reference signals, designated as "Sin" and "Cos" in Figure 3-2, are generated by a phase-locked-loop circuit which is synchronized to the function generator that drives the transmitter. The output of a phase-sensitive detector is a signal proportional to $A\sin\varphi$ or $A\cos\varphi$, depending on the phase of the reference signal ("Sin" or "Cos"), where A is the amplitude of the object wave and φ is, up to multiples of 2π, the phase with respect to the transmitted signal. Further details of the signal processing electronics are given in Appendix B.

To achieve large frame rates, all array signals are processed in parallel. Each of the 96 array elements has its own amplifiers and two phase-sensitive detectors. The active filter stage, however, contains only 24 parallel channels, limiting its usage to 24 elements at a time. The preamplifiers are located close to the array on 12 printed circuit boards. Their output signals are then high-pass

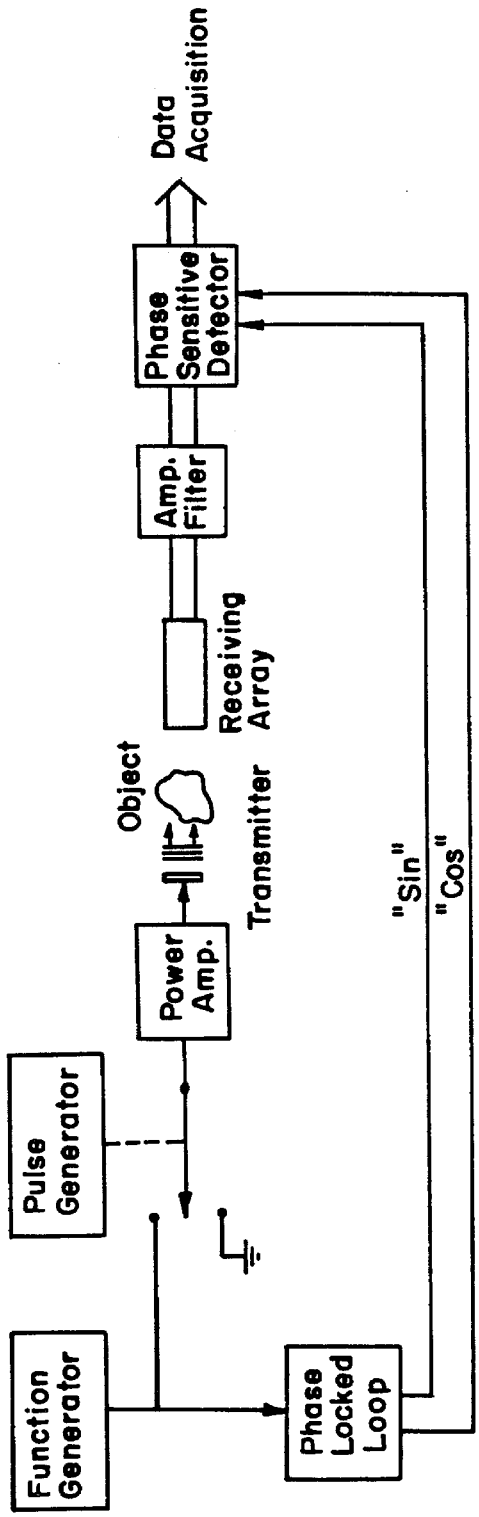

Figure 3-2. System Block Diagram

filtered and transferred to 24 processing printed circuit boards. Every board can process a maximum of four signals, i.e., it contains four amplifiers and eight phase-sensitive detector circuits. Prototypes of the circuit boards were designed, constructed, and tested with the help of the electronics shop of GAL-CIT. The production of all 12 preamplifier and 24 processing boards was then carried out by local electronics firms.

3.3. Data Acquisition

Each of the 24 processing printed circuit boards also contains one 8-bit A/D converter. An address generator provides an 8-bit address word that multiplexes the eight signal lines into one A/D converter and activates the output of one A/D converter at a time. While the next processing board is activated, the previous one has already started the conversion of its next data channel, such that the conversion is completed when this particular board is addressed again. The output of all A/D converters is transferred through a common data bus to a digital tape recorder (Kennedy, Incremental Magnetic Tape Recorder, Model 1600/360). Further processing of the magnetic tapes is then carried out on a PDP 11/44 computer. Additional details of the data acquisition electronics are described in Appendix C.

The interleaved data conversion and acquisition, combined with parallel signal processing described in the previous section, amount to a maximum frame rate of 2.5 kHz. Operating only 24 array elements at a time allows one to increase the frame rate to 10 kHz. In either operating mode, the respective maximum frame rate limits the object fluctuations that can be resolved by the system.

In most applications it will be necessary to operate the sound system in a pulsed mode in order to avoid standing waves between transmitter and receiving

array. The maximum frame rate is then limited by the highest possible pulse repetition rate assuming that only one data frame is acquired during every pulse. Even though the high data acquisition rate may freeze the object fluctuations, the repetition rate for consecutive data frames is generally limited by this operating procedure.

Chapter 4

APPLICATION TO A SWIRLING FLOW IN A DUCT

The concepts discussed in the previous chapters will now be applied to a swirling air flow in a circular duct. The aim of this experiment is to show the feasibility of using ultrasound as a means of measuring velocity disturbances. Since velocity changes are small compared to the speed of sound, most of the sound energy is transmitted through the flow. Hence, a transmission imaging technique is used.

4.1. Experimental Facility

Figure 4-1 shows a schematic of the experimental facility consisting of the six-inch diameter jet, the airfoil swirl generator, and the test section. The exit of the six-inch jet was modified with a flange to accommodate the airfoil swirl generator shown in Figure 4-2. The generator was on loan from the Illinois Institute of Technology where it was used for generation and management of swirling flows in confined streams (Ahmed, Wigeland & Nagib, 1976). Two NACA 0012 airfoils with a span of 2.75 inches and a chord length of 3 inches are supported by a shaft at the ¼-chord position and mounted in a six-inch diameter, six-inch long lucite duct. By setting the angle of attack of both airfoils to equal values with opposite signs, the two center tip vortices combine to form a vortex with a strong rotational core and a nearly potential outer part (Ahmed, Wigeland & Nagib, 1976).

The zero reading of the angle of attack is found by studying the wake of both airfoils acting as one wing, i.e., set always at the same angle of attack. Two pitot probes separated by approximately half the wake width are positioned

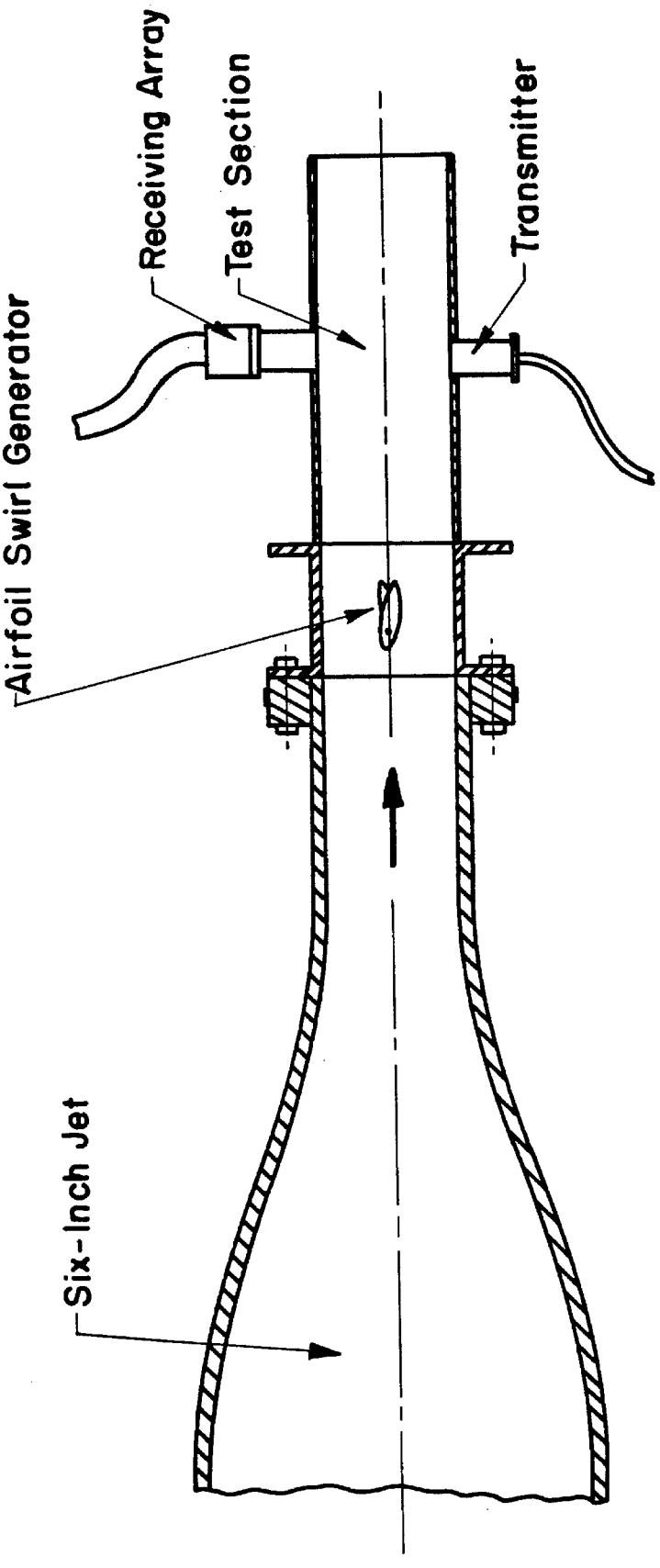

Figure 4-1. Experimental Facility (Top view)

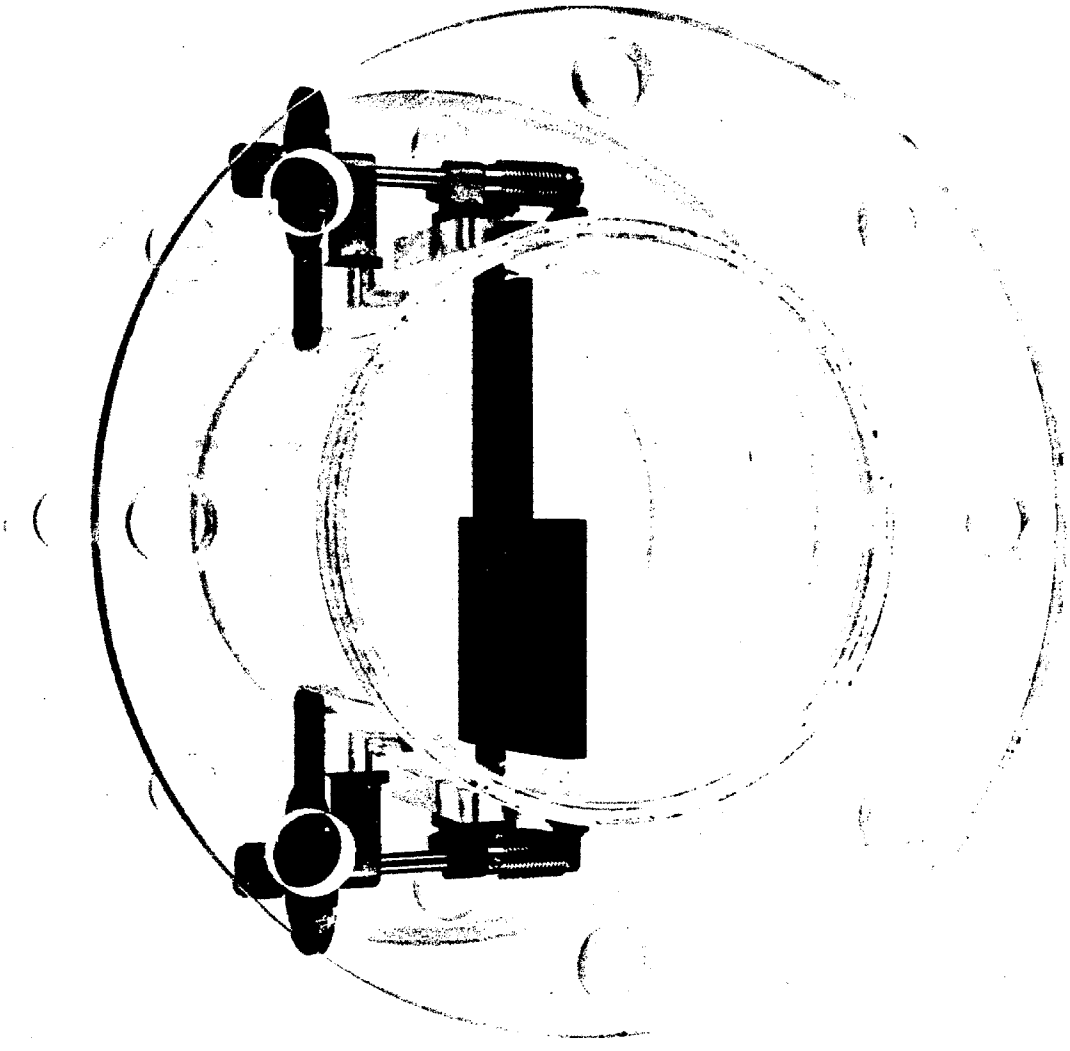

Figure 4-2. Airfoil Swirl Generator

symmetrically to the trailing edge and 1.25" downstream of the wings. Angle of attack and probe position are adjusted until the pressures on both probes are equal, indicating a symmetric wake and therefore a true zero angle of attack.

The test section is a 17.5-inch long mylar extension of the six-inch diameter duct. The acoustic transmitter-receiver assembly is located 10 inches downstream of the trailing edge of the wings. Both sensors are mounted rigidly on a common optical bench, as shown in Figure 4-3. The acoustic wave is propagating in the x-direction, perpendicular to the wingspan, in order to minimize the influence of the tip vortices at the outer edges of the wings. The mean flow is coming out of the plane in the z-direction and convects the entire sound beam downstream. In order to obtain maximum amplitude response, the array is positioned downstream of the transmitter accordingly by an amount Δz given by

$$\Delta z = \frac{U_\infty}{a_0} L \ , \tag{4-1}$$

where U_∞ is the free stream velocity, a_0 is the undisturbed speed of sound, and L the distance between transmitter and receiving array. Element numbers along the array increase in the y-direction.

Since the illuminating beam does not spread significantly over the six inches propagation length, it is sufficient to use only 24 elements (No. 27-50) of the receiving array, which results in a sensitive area of 0.84 x 0.5 inch. The plane sensors, which are positioned such that they cause a minimal deviation to the circular shape of the duct, are coupled directly to the air flow through holes cut into the mylar extension.

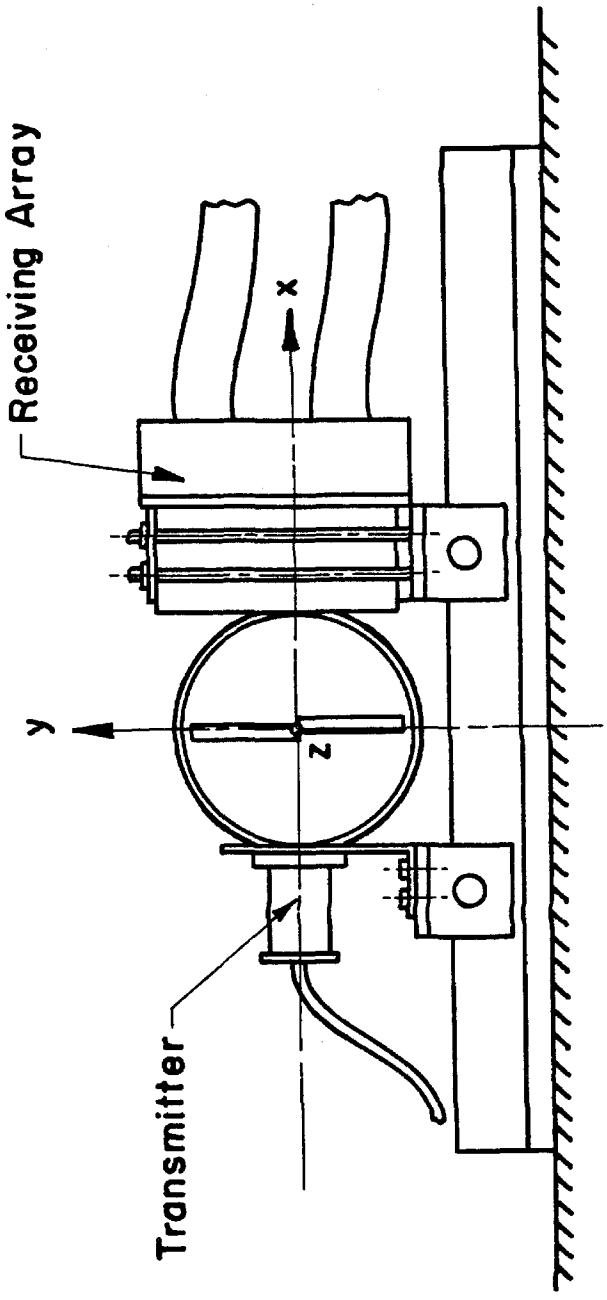

Figure 4-3. Transmitter-Receiver Assembly

To ensure single passage of a wavetrain through the test section, the sound system is operated in a pulsed mode. Each pulse is 400 μsec long, which is long enough to acquire at least one complete frame and short enough to avoid overlap with the first reflection from the wall. Consecutive pulses are only triggered after all reflections have died out.

The entire experimental procedure is as follows: After setting the angles of attack at the airfoil swirl generator, and after adjusting the jet velocity, a manually activated start signal triggers the data transfer to the digital tape recorder. The transmitting pulse is triggered 1750 μsec later to ensure that the processor is in a steady state cycling mode. Only one pulse is triggered during the recording of one record, resulting in one data frame out of 82 frames recorded per record. Then the system is cleared and a new set of data can be recorded. All measurements are taken at a frame rate of 8.3 kHz, which is equivalent to 120 μsec per frame.

4.2. Results

Before presenting the results, some general run and processing procedures are given in this section. Every run is started by taking one record of data without flow and without transmitting any sound. Ideally, all 82 frames contained in this record should have an output level of zero. However, there is a $\pm$ 1 bit variation due to slight offsets in the amplifier and low pass filter stages. An average is taken over all frames in this record resulting in a calibration frame given by

$$(A\sin\varphi)_{0j} = \frac{1}{82}\sum_{i=1}^{82}(A\sin\varphi)_{ij} \qquad (4\text{-}2)$$

$$(A\cos\varphi)_{0j} = \frac{1}{82}\sum_{i=1}^{82}(A\cos\varphi)_{ij} \ , \tag{4-3}$$

where i is the frame index and j the element index. This calibration frame is subtracted from all subsequent measurement frames.

$$(A\sin\varphi)_{ij} = (A\sin\varphi)'_{ij} - (A\sin\varphi)_{0j} \tag{4-4}$$

$$(A\cos\varphi)_{ij} = (A\cos\varphi)'_{ij} - (A\cos\varphi)_{0j} \ , \tag{4-5}$$

where the primed values are the actual measurement data. Amplitude and phase are then computed according to

$$A_{ij} = \sqrt{(A\sin\varphi)^2_{ij}+(A\cos\varphi)^2_{ij}} \tag{4-6}$$

$$\varphi_{ij} = \arctan\frac{(A\sin\varphi)_{ij}}{(A\cos\varphi)_{ij}} \ . \tag{4-7}$$

After acquiring the calibration record, the transmitter is turned on and 50 records of mean flow data are taken. This is accomplished by running the jet into the airfoil swirl generator with both half wings set at zero angle of attack. Finally, 50 records are taken with the half wings set at opposite angles of attack, which introduces the swirl in addition to the mean flow. Subtracting both sets of data from each other gives the swirling component alone. This was found to be the optimum procedure for the present experiment, since possible nonuniformities in the illuminating beam do not contribute to the swirling flow results.

In all measurement records, only one sound pulse is transmitted per record and only one data frame is used for subsequent processing. To make sure that this frame is acquired in the middle of the pulse, its data are compared with data immediately preceding and following that frame. Since the flow has not changed significantly during the acquisition time of one frame, each element should have roughly the same output. In carrying out this overlap check, an intermittent problem on the output of element 10 was discovered. Frames where this occurred were not used for further processing.

4.2.1. *Mean Flow Results.* Mean flow data (without swirl) are taken to establish reference data for the swirling flow component. Figure 4-4 shows the amplitude and phase distribution along the array for a free stream velocity, U_∞ = 75 ft/sec, averaged over 50 frames

$$A_j = \frac{1}{50} \sum_{i=1}^{50} A_{ij} \tag{4-8}$$

$$\varphi_j = \frac{1}{50} \sum_{i=1}^{50} \varphi_{ij} \tag{4-9}$$

and normalized with their respective mean values. The phase is plotted in radians, while units for the amplitude are arbitrary.

The amplitude distribution exhibits a broad peak centered around element 10. However, the peak is narrower than one would expect from diffraction theory, which is probably due to nonuniformities in the transmitter. The phase distribution shows a rather flat and slightly tilted region extending from element 4 to 19. Within this range the wave front is plane to less than 0.07 λ and propagates upward by 0.8°. However, outside of the region from element 4 to 19

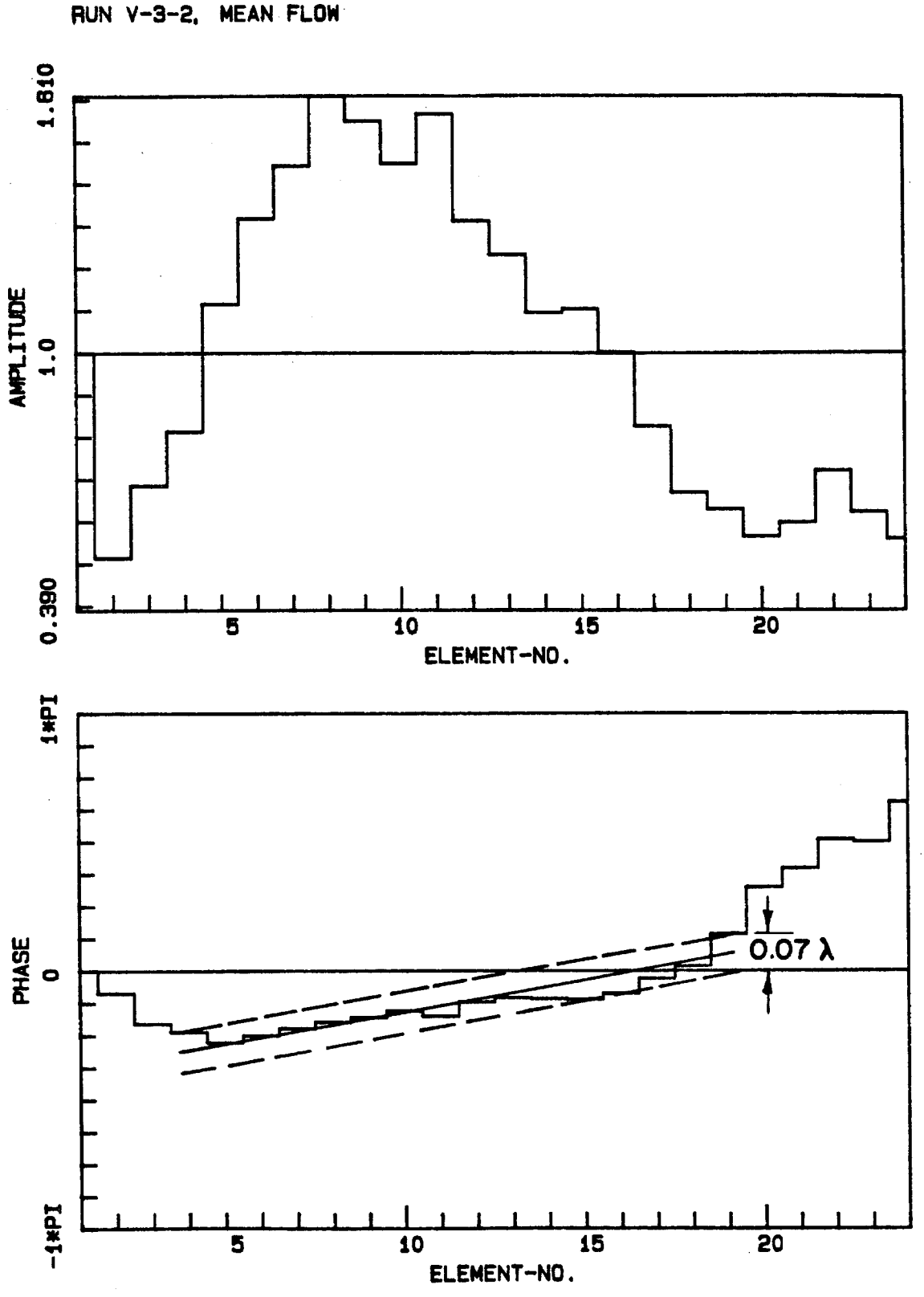

Figure 4-4. Amplitude and Phase Distribution for U_∞=75 ft/sec and α=± 0°

the wave front exhibits substantial curvature. Since the acoustic technique is only sensitive to the velocity component in the direction of wave propagation, the strongly curved part of the wave senses a different velocity component than the remaining wave front. Therefore, meaningful results can only be obtained where the wave front is plane.

It was mentioned earlier that amplitude and phase plots in Figure 4-4 are normalized with their respective mean values $\bar{A}$ and $\bar{\varphi}$ which are averages taken over all 24 elements, and given by

$$\bar{A} = \frac{1}{24} \sum_{j=1}^{24} A_j \ , \tag{4-10}$$

$$\bar{\varphi} = \frac{1}{24} \sum_{j=1}^{24} \varphi_j \ . \tag{4-11}$$

While amplitude normalization implies taking the ratio $\frac{A_j}{\bar{A}}$, the meaning of phase normalization is to subtract the mean value, $\bar{\varphi}$, from φ_j given in Equation (4-9). Closer examination of the mean phase for *individual* frames shows variations of $\sim 20°$, indicating a path length difference of 0.1 mm, which is caused by vibrations of the transmitter mounting bracket. The natural frequency of this L-shaped bracket is at least one order of magnitude lower than the frame rate, such that these mechanical vibrations do not interfere with the actual phase measurement. They merely cause a dc-shift of the phase signature over the entire array, which is subtracted as the mean value $\bar{\varphi}$. Besides these mean phase fluctuations, one can observe a downward trend of the mean values for individual frames by $\sim 45°$ over 30 min, indicating a slight increase in sound speed which translates into a heating of the air of 0.9°.

4.2.2. *Swirling Flow Results.* After establishing the "mean flow" reference conditions, 50 data frames are taken at the same free stream velocity U_∞=75 ft/sec, but with the wings of the airfoil swirl generator set at α=± 5°. This introduces a counterclockwise rotating vortex superimposed on the mean flow without causing a significant drop in the free stream velocity. Averaged amplitude and phase distributions along the array are normalized with their respective mean values (c.f. previous section) and plotted in Figure 4-5. The change from Figure 4-4 to Figure 4-5 is due to the vortex motion in the flow.

The amplitude distribution in Figure 4-5 shows a peak which is broader than in Figure 4-4, and which is shifted to the right. The entire sound beam is deflected upwards by the vortex motion because the incident beam width is of the same order as the size of the vortex. Furthermore, the strong departure of the mean flow amplitude distribution (Figure 4-4) from the "ideal" case, $A=const$, does not allow one to draw any further conclusions from the amplitude distribution in Figure 4-5. However, the phase distribution does indicate the presence of a vortical motion within the duct. Compared to Figure 4-4 the wave front is advanced on the lower and retarded on the upper end of the array indicating a counterclockwise rotation.

The upward deflection of the sound beam results in a very low system output $A\sin\varphi$ and $A\cos\varphi$ at the lower end of the array. The system output is so small that the quantization error in the A/D conversion causes large errors in the amplitude and phase computations. These errors, δA and $\delta\varphi$, can be estimated by taking the total differential of A and φ given in Equations (4-6) and (4-7) and allowing for small variations ε (=1 bit) in $A\sin\varphi$ and $A\cos\varphi$. The result depends, as expected, on the actual signal levels $A\sin\varphi$ and $A\cos\varphi$ and is given by

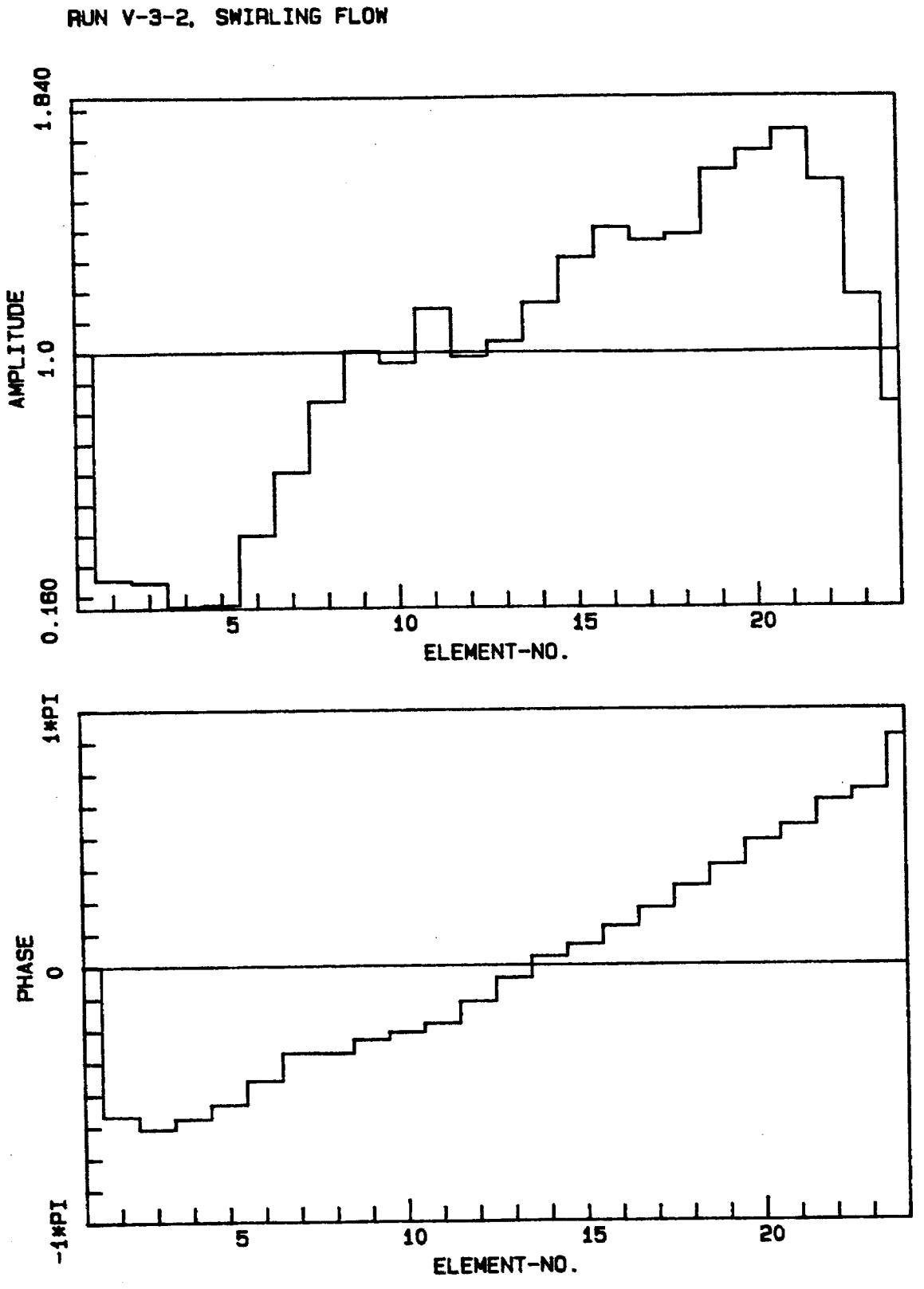

Figure 4-5. Amplitude and Phase Distribution for U_∞=75 ft/sec and α=± 5°

$$\left|\delta\varphi\right|_{max} = \left|\frac{\delta A}{A}\right|_{max} = \varepsilon \frac{|A\sin\varphi| + |A\cos\varphi|}{(A\sin\varphi)^2 + (A\cos\varphi)^2} , \qquad (4\text{-}12)$$

where the subscripts ij have been omitted. At element 4, where the amplitude has a minimum, the error has a maximum of 35% for the relative amplitude and 20° for the phase. Only for element numbers larger than 6 are the quantization errors within acceptable bounds: 3.5° for the phase and 6% for the amplitude.

The total quantization error, which is defined as the sum of the mean flow and the swirling flow error, is dominated by the latter contribution. Below element 7 the total phase error becomes larger than 5° and limits the effective array length on the lower end. On the upper end, the phase of the mean flow is strongly curved, which limits the effective array length to element numbers smaller than 20. Thus only elements 7-19 will be considered for further data processing.

Mean flow and swirling flow results, presented in Figures 4-4 and 4-5 respectively, are averages taken over 50 frames each. The root mean square phase fluctuations in both cases are of the order of 5° for most elements of the array, which is of the same order as the quantization error. (The rms fluctuations increase to $\sim 10°$ at the edge elements 7 and 19, where amplitudes are low.) Since the sound system is capable of tracking unsteady velocity fields, it can be concluded that the flow is extremely steady and presumably laminar.

The phase distribution due to the vortex alone is obtained by subtracting the phase distribution in Figure 4-4 from the one in Figure 4-5. This difference is processed with a running three-point average and normalized with its own mean value. The result, as plotted in Figure 4-6, shows a rather symmetric phase distribution over the effective array length that levels off on both sides.

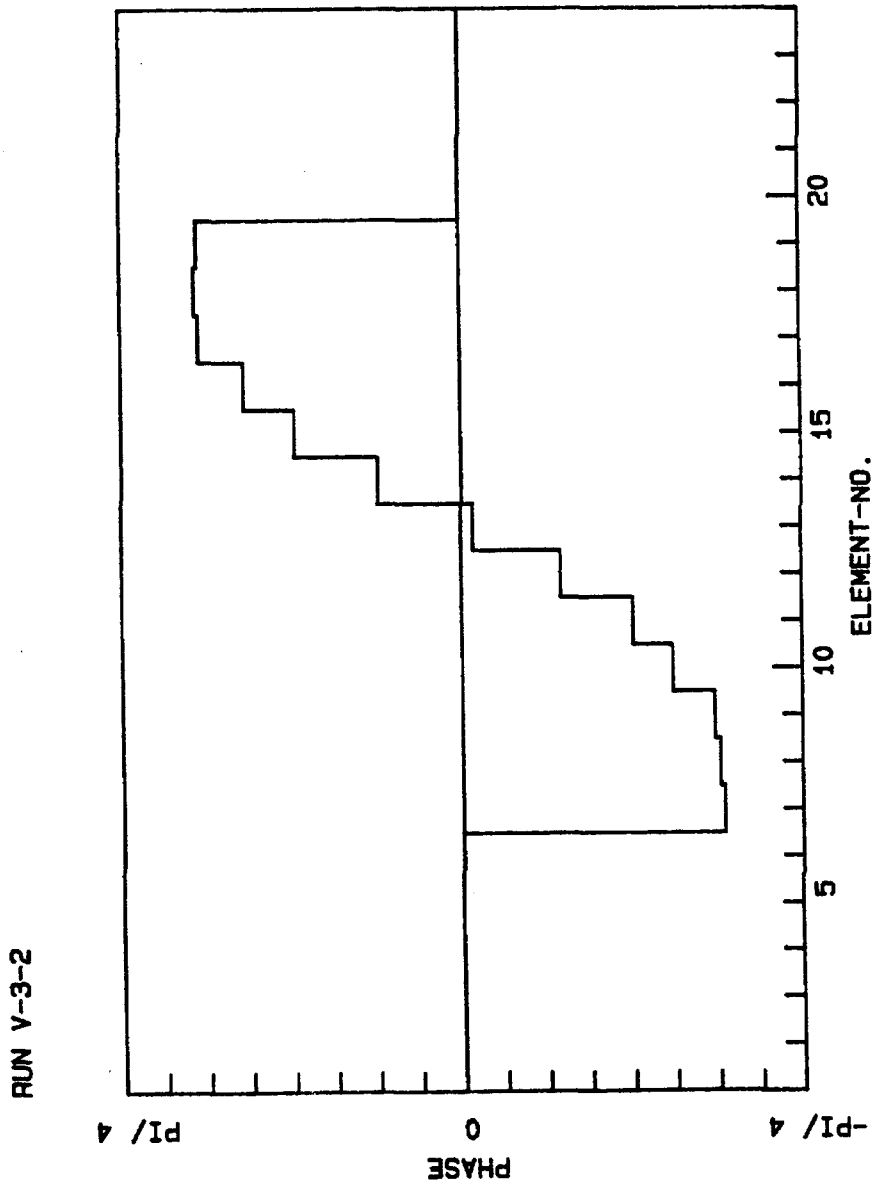

Figure 4-8. Phase Signature of a Vortex Generated with U_∞=75 ft/sec and $\alpha = \pm 5°$

Qualitative and limited quantitative information about the vortex can be obtained directly from the phase plot in Figure 4-6. The center of the vortex is located at the zero phase position, which is around element 13. A slight correction of ~ 1 element downward should be made for the slight upward tilt of the illuminating beam. Therefore, within the spatial resolution of the array, the vortex center is located at the center of the array which is also the center of the duct.

To deduce quantitative information about vortex size and strength directly from Figure 4-6 a velocity profile of the form

$$\frac{v(r)}{v_m} = 1.4\,\frac{r_0}{r}\left[1 - \exp\left[-1.26\,\frac{r^2}{r_0^2}\right]\right] \tag{4-13}$$

is assumed which will be referred to as exponential fit. Here, r_0 is the so-called "inner core radius," where the tangential velocity, v, attains its maximum value v_m. The exponential fit was chosen for its simplicity in describing the velocity profile of a vortex continuously for all r: Solid body rotation near the center and a potential vortex for large r. Equation (4-13) is also the solution of a viscous rectilinear vortex (Eskinazi, 1967) when normalized with v_m and r_0. It is conceivable that a better fit could be obtained with the Saffman vortex (Saffman, 1978), which has more adjustable parameters. However, this requires extensive numerical studies while the exponential fit can be integrated in closed form. Substituting Equation (4-13) into Equation (2-4) and integrating from minus to plus infinity, one obtains for the phase shift

$$\Delta\varphi(y) = -\frac{\Gamma}{2}\,\frac{k_0}{a_0}\,\mathrm{erf}\left[\sqrt{1.26}\,\frac{y}{r_0}\right], \tag{4-14}$$

where, Γ, the circulation of the vortex is related to r_0 and v_m by $\Gamma = 2.8\pi r_0 v_m$ (see Appendix D). The value of $\Delta\varphi$ reaches 99.5% of its maximum at approximately 1.8 r_0. Since the measured phase distribution in Figure 4-6 suggests a functional form like that of Equation (4-14), the circulation, Γ, can be estimated by

$$\Gamma = -\Delta\Phi \frac{a_0}{k_0}, \tag{4-15}$$

where $\Delta\Phi$ is the peak-to-peak phase difference in Figure 4-6. If $\Delta\Phi$ is replaced by the expression $k_0 a_0 \Delta t$, where Δt is the corresponding time of flight difference, Equation (4-15) is identical with Equation (1a) derived by Schmidt (1975), who integrated the velocity field in the potential region on either side of the vortex.

The inner core radius, r_0, can be deduced from the center slope of the phase distribution, $\Delta\varphi$. Taking the derivative of Equation (4-14) at $y=0$ and using Equation (4-15) one obtains

$$r_0 = 0.635\ \Delta\Phi \left[\frac{d\Delta\varphi}{dy}\bigg|_{y=0} \right]^{-1}. \tag{4-16}$$

With Equations (4-15) and (4-16) all vortex parameters can be determined from Figure 4-6. One calculates an inner core radius of 3.25 mm and a circulation of -0.12 m^2/sec, resulting in a maximum velocity of -4.2 m/sec, where the minus-sign indicates that the vortex is rotating counterclockwise.

Finally, the radius of curvature of the transmitted wave front is a measure for the distance at which focusing occurs. After dividing Equation (4-14) by k_0 one computes a focal length

$$F = \frac{\left[1 + \frac{1.26\,\Gamma^2}{\pi r_0^2 a_0^2} \exp\left[-2.52\,\frac{y^2}{r_0^2}\right]\right]^{3/2}}{\left[\frac{8}{\pi}\right]^{1/2} \frac{\Gamma y}{r_0^3 a_0} \exp\left[-1.26\,\frac{y^2}{r_0^2}\right]} . \qquad (4\text{-}17)$$

An order of magnitude estimate yields

$$\frac{F}{r_0} \sim \frac{a_0}{v_m} , \qquad (4\text{-}18)$$

where $F \sim 10''$ for the vortex under investigation. To avoid focusing, the measuring station has to be located less than 10" away from the vortex center. With this distance being 3" in the present experiment the above condition is satisfied.

4.3. Digital Reconstruction of Tangential Velocity Profile

If a more detailed knowledge about the velocity field is required, it becomes necessary to employ digital reconstruction techniques. Assuming that the flow is rotationally symmetric, the Abel inversion as described in Section 2.3 may be used to reconstruct the entire tangential velocity profile. However, in the present experiment, phase measurements were made only in the central region of the circular test section, and it is only in this region where one can expect good results.

The Abel inversion formula was given as Equation (2-6) where $\Delta\varphi(y)$ is the phase distribution in Figure 4-6. Since the integral involves only half of the measured phase data, an average between elements equidistant from the centerline, i.e. element 13, has been taken. Fitting a fourth order polynomial through the resulting data points leads to Figure 4-7, where y is normalized with the element spacing, s. The error bars represent the quantization errors as

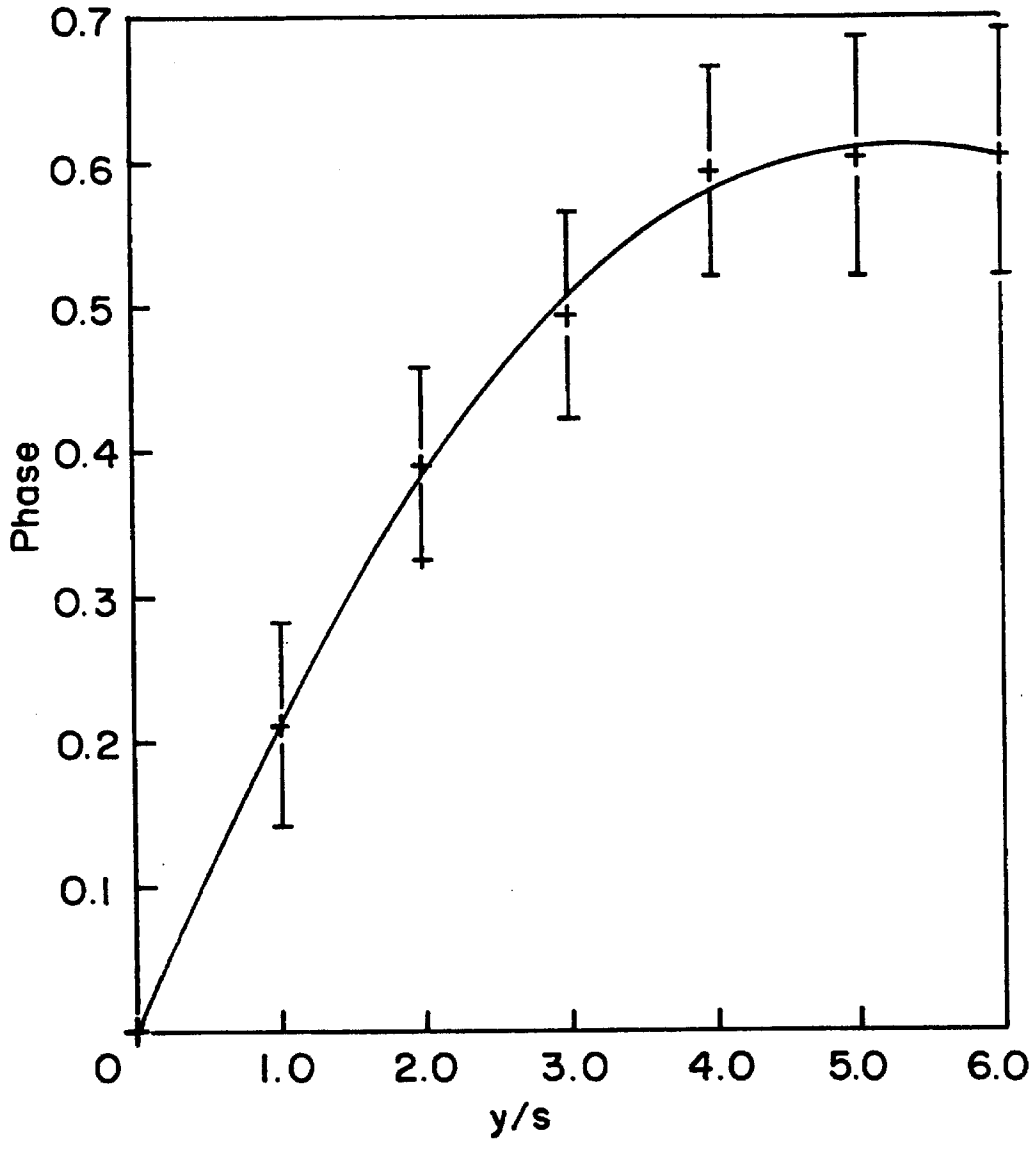

Figure 4-7. Input Phase Distribution for Abel Inversion

computed from Equation (4-12).

Looking back once more to Equation (2-6), it becomes apparent that the upper limit of the integral requires an extrapolation of $\Delta\varphi(y)$ beyond the measurement range. Since the phase distribution does level off at $\sim \frac{y}{s} = 5$, the considerations at the end of the previous section indicate that the velocity has settled down to a $\frac{1}{r}$ profile. Therefore, $\Delta\varphi(y)$ is extrapolated by a phase distribution resulting from $v \sim \frac{1}{r}$ which is calculated from Equation (2-5). With R being the radius of the circular duct the result is

$$\Delta\varphi(y) = -\,const\ \arctan\left[\frac{R^2-y^2}{y^2}\right]^{\frac{1}{2}}, \qquad (4\text{-}19)$$

where the *const* is determined by matching Equation (4-19) at $\frac{y}{s} = 6$ to the measurement data.

It was mentioned earlier that the phase distribution is weighted by $\frac{1}{y}$, which makes the phase extrapolation less important for larger y. The main contribution to the Abel integral always comes from the first few integration steps. For example, $\sim 75\%$ of the total reconstructed velocity at $\frac{r}{s} = 3$ comes from the integral within $3 \leq \frac{y}{s} \leq 6$. Therefore, a slightly different extrapolation will not significantly alter the reconstruction near the center.

Finally, performing the Abel inversion on the phase distribution in Figure 4-7, extrapolated according to Equation (4-19), results in the tangential velocity profile given in Figure 4-8. Plotted is $-v$, indicating that the vortex is rotating counterclockwise, versus $\frac{r}{s}$, where s is the element spacing. A step size of $\frac{1}{4}s$

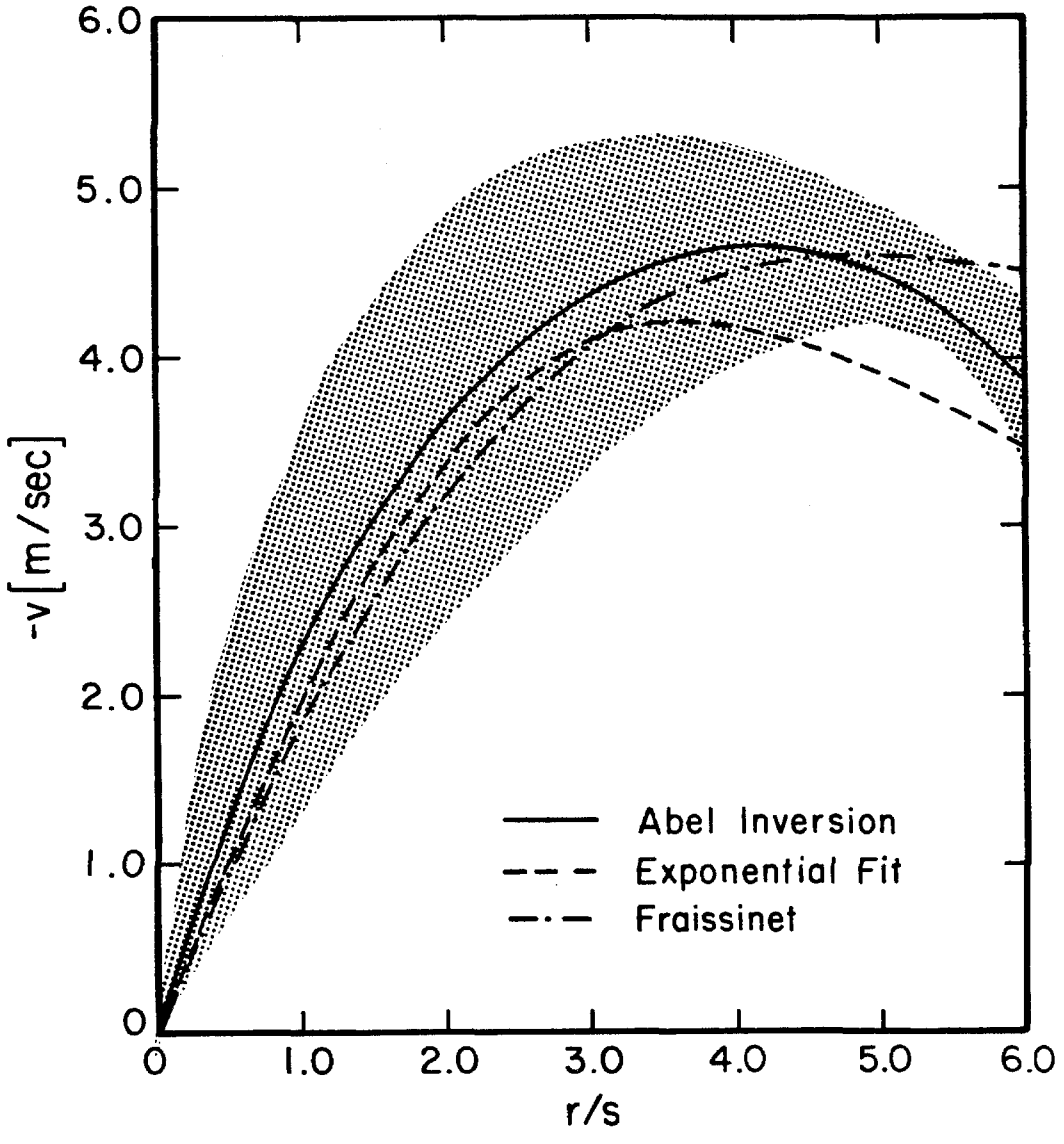

Figure 4-8. Tangential Velocity Profile

was chosen to give a sufficiently smooth reconstruction, showing a distinct peak at $r_0 = 4.2s$, where the velocity $v_m = -4.65$ m/sec. The dotted area represents the uncertainty in the reconstruction due to the error bars in Figure 4-7. It should be noted that the boundaries of this area result from computations of the worst possible cases. These imply no error on the center line ($y=0$) and errors of opposite sign for $y > 0$ and $y < 0$ respectively.

Figure 4-8 also contains an exponential fit according to Equation (4-13) with r_0 and v_m determined in the previous section directly from the phase signature in Figure 4-6. While the inner core radius is only slightly smaller, the maximum velocity is ~ 10% smaller than that of the reconstructed profile.

The third profile in Figure 4-8 is an average over two traces taken by Fraissinet (1976), who measured the tangential velocity by traversing a hot wire radially through the test section. The vortex was generated by the same airfoil swirl generator under the same flow conditions as in the present experiment. Even though measurements were taken 8" downstream of the trailing edge of the wings, the flow field is not significantly different at the present measuring station 10" downstream of the wings (Ahmed, Wigeland & Nagib, 1976). However, for $r > r_0$ the hot wire profiles become significantly asymmetric, which could be due to inaccuracies in the linearization of the hot wire calibration (Nagib, 1982, private communication). Keeping that in mind, the agreement between the hot wire data and the digital reconstruction by Abel inversion is rather good. The maximum velocity is predicted very accurately, while the predicted inner core radius is too small by less than one element spacing.

In summary, Figure 4-8 shows the importance of digitally reconstructing the velocity field. Modelling the vortex by Equation (4-13) just gives a quick indication of vortex size and strength.

Chapter 5

CONCLUSION AND OUTLOOK

An acoustic imaging system operating at 186 kHz and consisting of a 1" diameter transmitter and a 3.5" long 100-element piezoelectric receiving array was constructed. The signal processing and data acquisition electronics were designed to allow a maximum frame rate of 10 kHz in the 24-element mode. Real and imaginary parts of the transmitted wave are recorded on magnetic tape and further digital processing is carried out on a PDP 11/44 computer.

Objects of interest in the present work are gas flows, where the sound convection due to velocities dominates compared to changes in sound speed due to temperatures. The feasibility of measuring velocity disturbances with ultrasound was demonstrated by transmitting sound through a vortex which was generated in a circular duct by an airfoil swirl generator. Assuming an exponential fit for the tangential velocity component, inner core radius and circulation can be determined dirctly from the phase change of the transmitted wave due to the vortex. A more accurate representation of the tangential velocity profile can be found by digital reconstruction via the Abel inversion formula.

Even though the flow field under investigation was steady, it is important to note that this is neither a restriction of the acoustic technique nor of the apparatus. However, in most cases the necessary pulsed mode operation limits the repetition rate for consecutive data frames. A further application could consist of tracking large scale vortices in unsteady flows. In all these cases, temperature fluctuations have to remain small in order to avoid a superposition on the velocity effects. On the other hand, when the change of sound speed due

to temperatures is large compared to the sound convection due to velocities, an acoustic technique offers the possibility of making nonintrusive temperature measurements. A possible application of this method to reacting shear flows will be the subject of future studies.

6. References

AHMED, M., WIGELAND, R.A. & NAGIB, H.M. 1976 Generation and management of swirling flows in confined streams. I.I.T. Fluids & Heat Transfer Report, R76-2.

ENGLER, R.H. & SCHMIDT, D.W. 1979 Untersuchung des von einem Tragfluegelmodell im Windkanal erzeugten Wirbelfeldes mittels Ultraschallimpulsen. Mitteilungen aus dem Max-Planck-Institut fuer Stroemungsforschung, Nr. 69.

ENGLER, R.H., SCHMIDT, D.W., WAGNER, W.J. & WEITEMEIER, B. 1982 Ultrasonic method for flow field measurement in wind tunnel tests. *J. Acoust. Soc. Am.*, **71**, 42-50.

ESKINAZI, S. 1967 Vector Mechanics of Fluids and Magnetofluids. Academic Press, New York.

FRAISSINET, A. 1976 Turbulence decay downstream of manipulators and calibration of vane indicator rotation in swirling flows using an X-wire. I.I.T. Internal Report.

GOODERUM, P.B. & WOOD, G.P. 1950 Density fields around a sphere at Mach numbers 1.3 and 1.62. NACA, Technical Note 2173.

GRADSHTEYN, I.S. & RYZHIK, I.W. 1965 Table of Integrals, Series and Products. Academic Press, New York.

JOHNSON, S.A., GREENLEAF, J.F., HANSEN, C.R., SAMAYOA, W.F., TANAKA, M., LENT, A., CHRISTENSEN, D.A. & WOOLLEY, R.L. 1976 Reconstructing three-dimensional fluid velocity vector fields from acoustic transmission measurements. *Acoustical Holography*, **7**, 307-326.

KRAUTKRAEMER, J. & H. 1969 Ultrasonic Testing of Materials. Springer-Verlag, New York.

SAFFMAN, P.G. 1978 The number of waves on unstable vortex rings. *J. Fluid Mech.*, **84**, 625-639.

SCHMIDT, D.W. 1975 Akustische Messung der Zirkulation von Wirbeln und von Zirkulationsverteilungen bei Modelluntersuchungen in Windkanaelen. Mitteilungen aus dem Max-Planck-Institut fuer Stroemungsforschung und der Aerodynamischen Versuchsanstalt, Nr. 61.

SOLOMON, G. 1953 Transonic Flow Past Cone-Cylinders. C.I.T. Doctoral Dissertation.

Appendix A

RECEIVING ARRAY

This appendix describes some details of the receiving array construction. The pressure sensitive part is machined out of two silverplated piezoceramic plates 1.75 x 0.5 x 0.027 inch (Lead Zirconate Titanate, Glennite G1408), which are moulded in a 7 x 2.5 x 3 inch aluminum housing.

To have the back side of both plates act as a common ground, an electrical connection is made with a ¼-inch wide copper strip which is attached to both pieces with conductive epoxy. Furthermore, a sufficiently long copper strip is conductive epoxied at both ends of the extended plate. This assembly is then put at the bottom of a 1.5-inch high mould which is subsequently filled with the backing material consisting of epoxy (Emerson & Cuming, Inc., Stycast 1264) and glass balloons (~ 100 μ diameter) at a volume ratio of 3:4.

The individual elements are formed by milling transverse cuts, 0.008 inch wide, half way through the piezoceramic plate. The spacing between the cuts is 0.035 inch resulting in an array with a total of 100 elements. During the machining the plates were submerged in a water bath in order to keep the temperature below the Curie temperature (> 300°C for G1408), at which the material loses its piezoelectricity.

For transmission of the pressure signals a 0.005-inch diameter tinned copper lead is soldered to alternate edges of neighbouring array elements (see Figure 3-1). Even though the ceramic might lose some of its piezoelectricity locally due to the soldering, the better mechanical strength of the joint makes it preferable to using conductive epoxy.

The pressure sensitive area is protected by a ¾λ-thick layer of epoxy (Stycast 1264), which also provides a better acoustic impedance match between the ceramic and the working medium air. The thickness of this layer is controlled by spacers, which lift the array up from the bottom of the mould. To avoid air bubbles in the epoxy, it is evacuated for approximately one hour before pouring it into the mould.

Finally, all leads receive teflon sleeves and are soldered to a 100-pin connector on the back side of the array. The whole assembly is then inserted in a 7 x 2.5 x 3 inch aluminum housing, which is connected to the common ground before being filled with epoxy (Stycast 1264).

Appendix B

SIGNAL PROCESSING ELECTRONICS

Some details of the signal processing electronics will be described in this appendix. The processing system is divided into three stages: preamplifier, active filter, and main processing stage. In order to avoid ground loop problems, every stage is designed in a differential-input configuration.

The preamplifier stage consists of a low noise inverting operational amplifier circuit (National, LF357) with a gain of 30 followed by an emitter follower. The subsequent active filter stage contains second-order Butterworth high-pass filters with a cutoff frequency of 100 kHz and a gain of 2. The preamplifier and active filter stages are positioned close to the array and an emitter follower drives the signal lines, which go to the main processing stage. Its input is ac-coupled to an inverting operational amplifier circuit of gain 60 with high gain-bandwidth product (Harris, HA2627).

A phase-sensitive detector circuit, which is shown schematically in Figure B-1, is the central part of the main processing stage. An analog switch (Motorola, MC14551), which is activated by a reference signal E_R, passes either the amplified signal E_S or no signal at all. If E_R and E_S are of the same frequency, one obtains, after low-pass filtering E_{LP}, a dc output signal E_O which is proportional to the amplitude of E_S and to the phase of E_S relative to E_R. The filter is a second-order Butterworth filter with a cutoff frequency of 2 kHz and a gain of 6, allowing amplitude and phase changes up to 2 kHz to be recognized.

To demonstrate the phase dependence, Figure B-1 also shows three examples of phase relationships between E_R and E_S. If the input signal, E_S, is sinusoidal

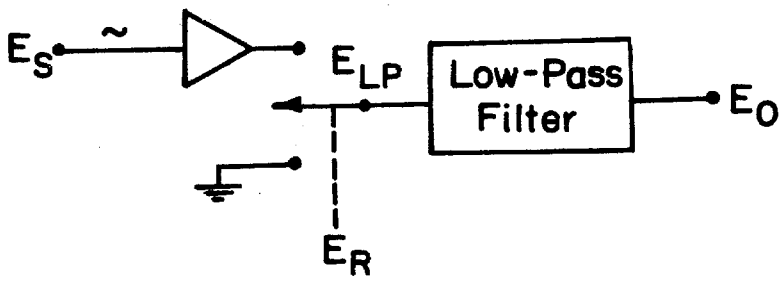

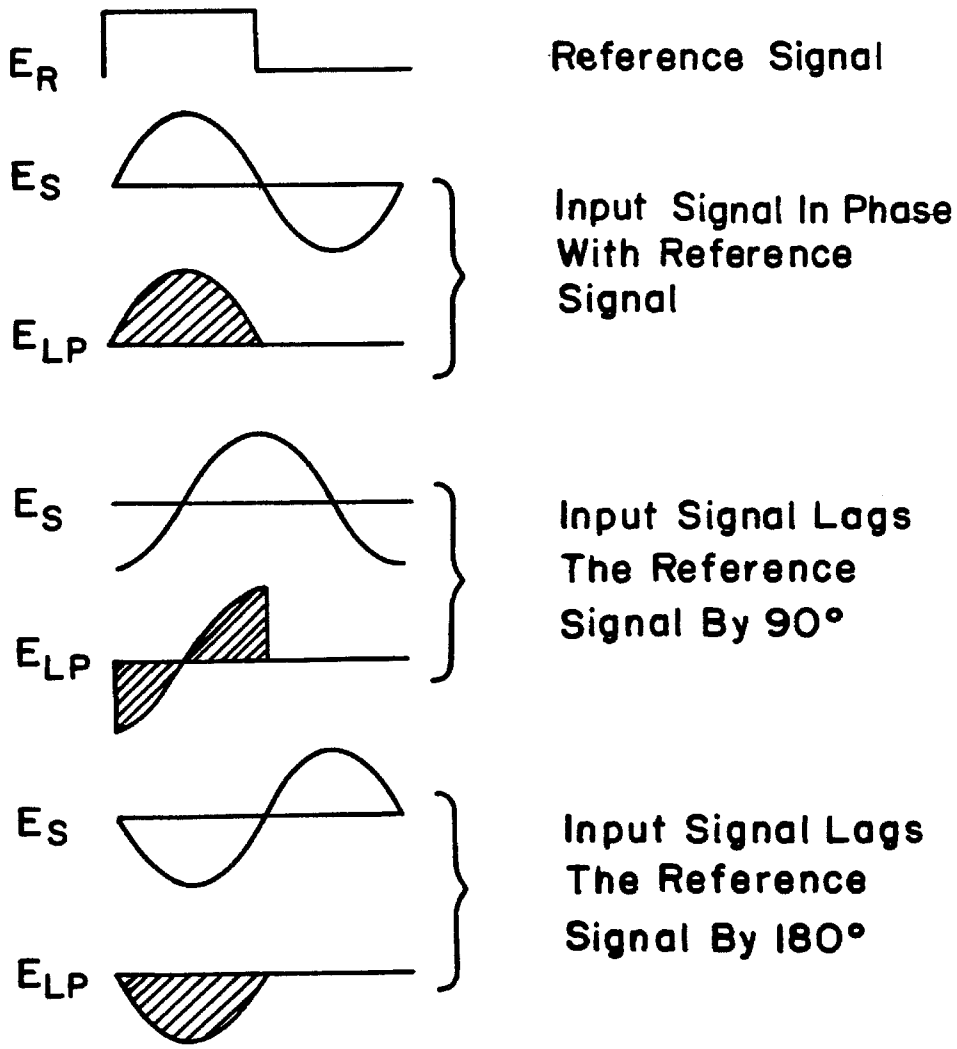

Figure B-1. Phase-Sensitive Detector Circuit

with amplitude A and in phase with the reference signal, E_R, the output signal, E_O, is proportional to the area under the first half cycle of the sinusoid, which is $\frac{A}{\pi}$. Similarly, if the same input signal lags the reference signal by 90°, the resulting output signal is zero. For a phase lag of 180°, one obtains $-\frac{A}{\pi}$. Amplitude and phase of E_S can be determined uniquely by mixing E_S with two reference signals, one being in phase and the other one leading by 90° with respect to the driving signal of the transmitter. The former operation results in a signal proportional to $A\sin\varphi$, the latter one to $A\cos\varphi$ where φ is, up to multiples of 2π, the phase angle between the transmitted and received signal.

The two reference signals at quadrature are generated by a digital phase-locked-loop circuit (RCA, CD4046). The sinusoidal transmitter signal is converted to a 10 V square wave, which serves as the input to the phase-locked-loop shown in Figure B-2. Two D-type flip-flops (CD4013) are arranged in the loop as follows: The voltage-controlled oscillator (VCO) output is fed into the clock (CK) input of flip-flop 1 (FF1) and after inversion into the clock input of flip-flop 2 (FF2). Flip-flop 1 divides the VCO frequency by two and closes the loop. This signal is in phase with the input signal and designated as "Sin". Connecting the inverting output of flip-flop 1 to the D inputs of both flip-flops results in an inverting output on flip-flop 2 which leads the input signal by 90°. These signals are then reduced to TTL levels and serve as reference signals in the phase-sensitive detector circuits.

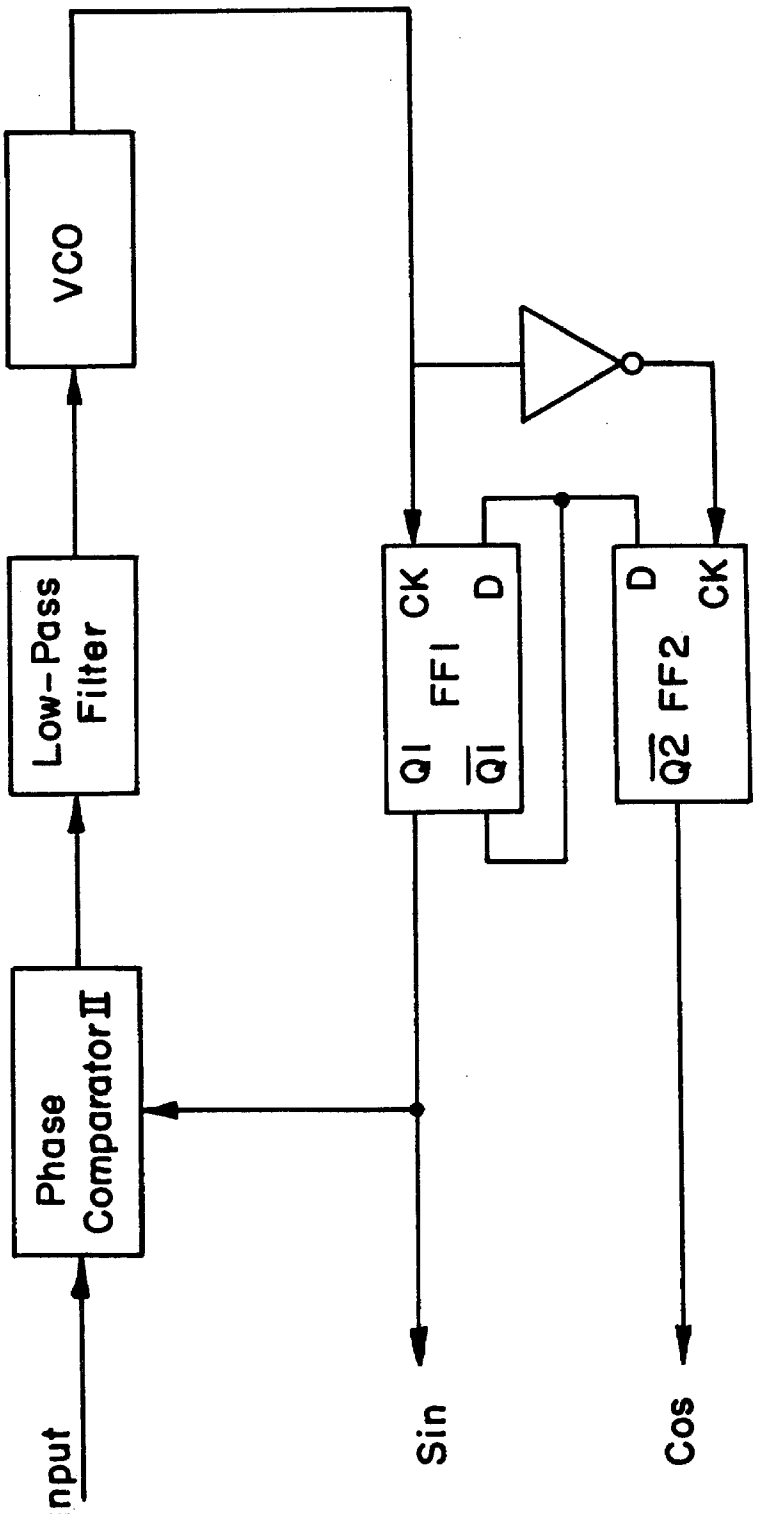

Figure B-2. Phase-Locked-Loop Circuit for Generating Reference Signals

Appendix C

DATA ACQUISITION ELECTRONICS

This appendix describes the details of the data acquisition electronics. First, the output signals of the phase-sensitive detectors are converted into an 8-bit word. The A/D converter (Analog Devices, AD570) is connected for bipolar operation with a typical full scale calibration error of ± 2 bits. Overall noise and crosstalk between adjacent channels are below ± 1 bit.

Then, to achieve a high frame rate, all signals are processed in parallel, i.e., every output signal has its own amplifier and phase-sensitive detector circuits. Always four preamplified and active filtered signals are transferred to one main processing board, as shown in Figure C-1. Each of the 24 processing boards contains eight phase-sensitive detectors which are multiplexed (Motorola, MC 14051) into one 8-bit A/D converter.

An address generator consisting of two independent down-counters supplies an 8-bit address word, in which the four least significant bits identify a particular processing board, while the four most significant bits represent the channel identification on the processing boards. Maximum channel and board identification numbers to be used can be preset to any desired value. As the address changes, a decoder on every board compares the four least significant bits of the address with the board identification numbers. On the particular board where both agree, the digital output is activated and then transferred through a common data bus to a high speed buffer memory and subsequently to the digital tape recorder (Kennedy, Incremental Magnetic Tape Recorder, Model 1600/360). As the address activates the next processing board, the previous one starts a new conversion, after which a shift register multiplexes the next

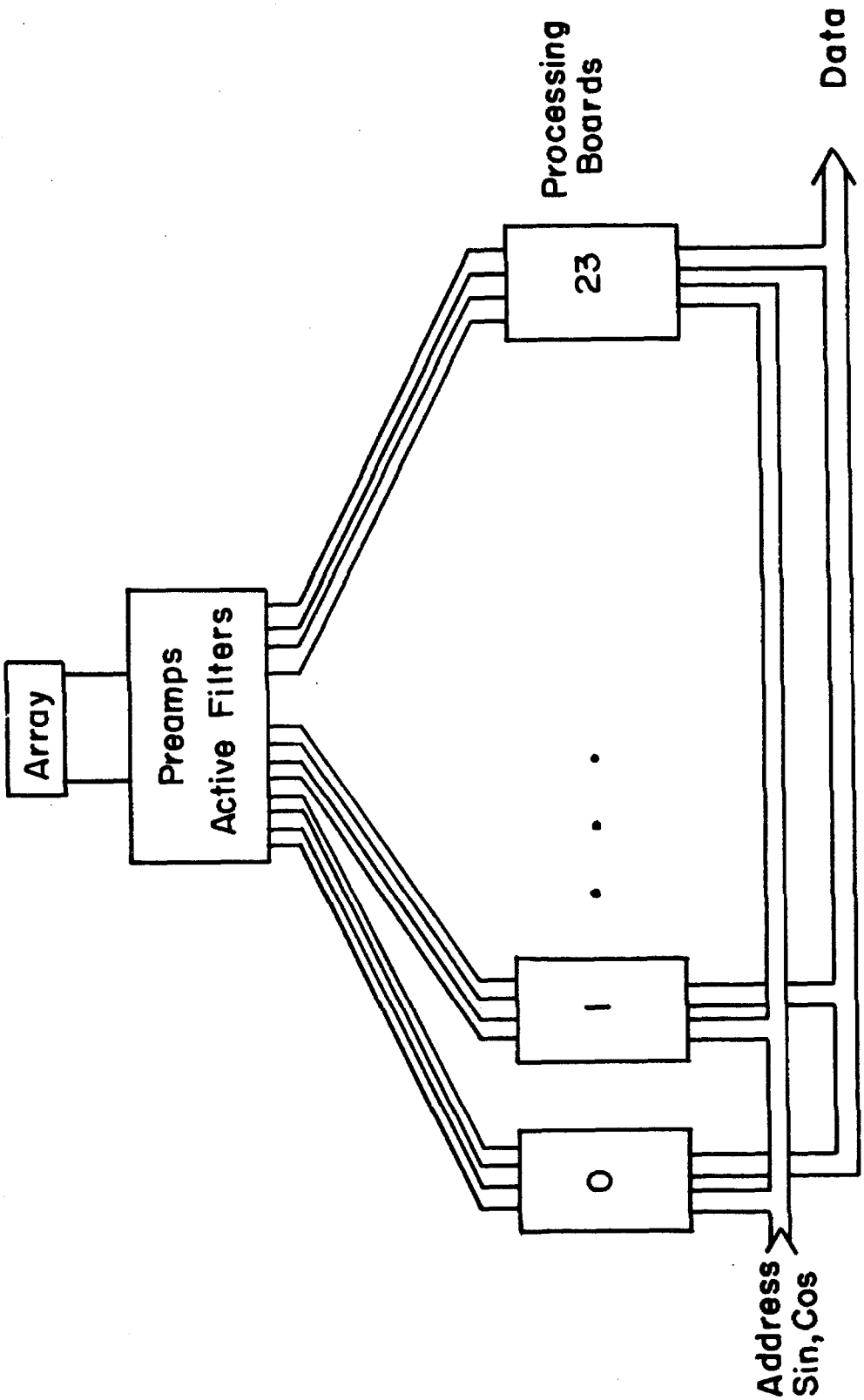

Figure C-1. Structure of Processing Electronics

channel output onto the A/D converter. Since data transfer to tape and A/D conversion take place at the same time, one can obtain higher frame rates than in a sequential process.

When the address generator is preset to a specified value before starting the counters, there exists a unique relationship between the address and the corresponding array element number, whose processed signal is at that time present at the output. Hence, the corresponding element numbers can be determined from the string of output data alone. An additional check is arranged by hardwiring the outputs of element 1 to ± 5 V, which mark the beginning of a new frame on the data records.

The maximum frame rate for a given number of elements in use is limited by a 5 μsec convert pulse plus the A/D conversion time ($\sim$ 45 μsec maximum), and the number of channels per board (=8 in the 96 element mode). Therefore, the maximum frame rate utilizing the entire array amounts to 2.5 kHz. However, in the 24 element mode every signal line has its own processing board, i.e., only two channels per board are in use. This increases the maximum frame rate to 10 kHz.

Finally, the 24 processing boards are arranged in two racks of 12 boards each operating in parallel. Both 8-bit data busses are combined into one 16-bit bus for transfer to the buffer memory. This does not increase the maximum frame rate, but reduces the corresponding maximum addressing frequency by a factor of ½, i.e., in the 24 element mode from 480 kHz to 240 kHz.

Appendix D

STRAIGHT RAY INTEGRATION

This appendix contains the derivation of Equation (4-14), which describes the phase shift of a transmitted sound wave due to a rotationally symmetric velocity field given by Equation (4-13). Here $v(r)$ is the tangential velocity of a vortex with a maximum value v_m at $r=r_0$. For $r>>r_0$, the velocity approaches $1.4\, v_m \frac{r_0}{r}$, which has the functional form of a potential vortex with circulation

$$\Gamma = 2.8\pi r_0 v_m \ . \tag{D-1}$$

Substituting Equation (4.13) into Equation (2-4) with infinite integration limits gives

$$\frac{\Delta\varphi(y)}{y} = -1.4\, v_m \frac{k_0 r_0}{a_0} \int_{-\infty}^{\infty} \frac{1}{r^2} \left[1 - \exp\left[-1.26 \frac{r^2}{r_0^2} \right] \right] dx \ . \tag{D-2}$$

Introducing $r^2=x^2+y^2$ and making use of the symmetry of the integrand with respect to x reduces the solution of Equation (D-2) to solving the following two integrals:

$$\int_0^{\infty} \frac{dx}{x^2+y^2} = \frac{\pi}{2y} \tag{D-3}$$

$$\int_0^{\infty} \exp\left[-\frac{1.26}{r_0^2}(x^2+y^2) \right] \frac{dx}{x^2+y^2} = \left[1 - \operatorname{erf}\left[\sqrt{1.26}\, \frac{y}{r_0} \right] \right] \frac{\pi}{2y} . \tag{D-4}$$

The integral in Equation (D-4) is of the same form as No. 3.466-1. in Gradshteyn and Ryzhik (1965). By substituting Equation (D-3) and (D-4) into Equation (D-2) one obtains

$$\Delta\varphi(y) = -1.4\pi r_0 v_m \frac{k_0}{a_0} \operatorname{erf}\left[\sqrt{1.26}\,\frac{y}{r_0}\right]. \qquad \text{(D-5)}$$

Finally, using Equation (D-1) leads to Equation (4-14).

Engler et al. (1982) carried out a similar calculation by numerical means without linearizing the acoustical index of refraction. Their Figure 2 gives the time-of-flight difference, $\Delta t_{\#}$, versus y and shows two distinct peaks, whose position is proportional to the inner core radius, r_0 (Engler & Schmidt, 1979). It can be shown that these peaks are introduced by finite integration limits in Equation (D-2) and that the proportionality factor of r_0 depends on the actual integration length. No such distinct peaks appear in the present measurements because the probes are located in the far field of the vortex, i.e., the probe separation, L, is much larger than $2r_0$.

Appendix E

PLUME EXPERIMENT

When the change of sound speed due to temperatures is large compared to the sound convection due to velocities, an acoustic technique offers the possibility of making nonintrusive temperature measurements. This is demonstrated by transmitting ultrasound through a temperature-driven axisymmetric plume in water.

The schematic of the experiment is given in Figure E-1. The top view on the water tank shows the plume which is generated by a heater at the bottom of the tank, the mechanical traverse and the transmitter-receiver assembly. A piezoelectric probe, 2 mm in diameter, is used as the transmitter and is rigidly connected by a U-shaped arm to a 0.8 mm diameter receiving probe, 13" away. The entire unit is traversed through the tank at a height of 4" above the bottom and 5" below the water surface such that the receiver is always ~ 6.5" away from the plume.

In order to avoid interference from wall reflections with the wave traveling directly to the receiver, the system is operated in a pulsed mode. Sine-wave bursts of 3 MHz frequency and 50 μsec duration with 1.8 kHz repetition rate are generated by a function generator, which is triggered by a pulse generator. The signal at the receiving probe is amplified and bandpass filtered before being passed through a true rms voltmeter, whose output is proportional to the amplitude of the received sound bursts. Finally, this amplitude is recorded as a function of position on a X-Y plotter.

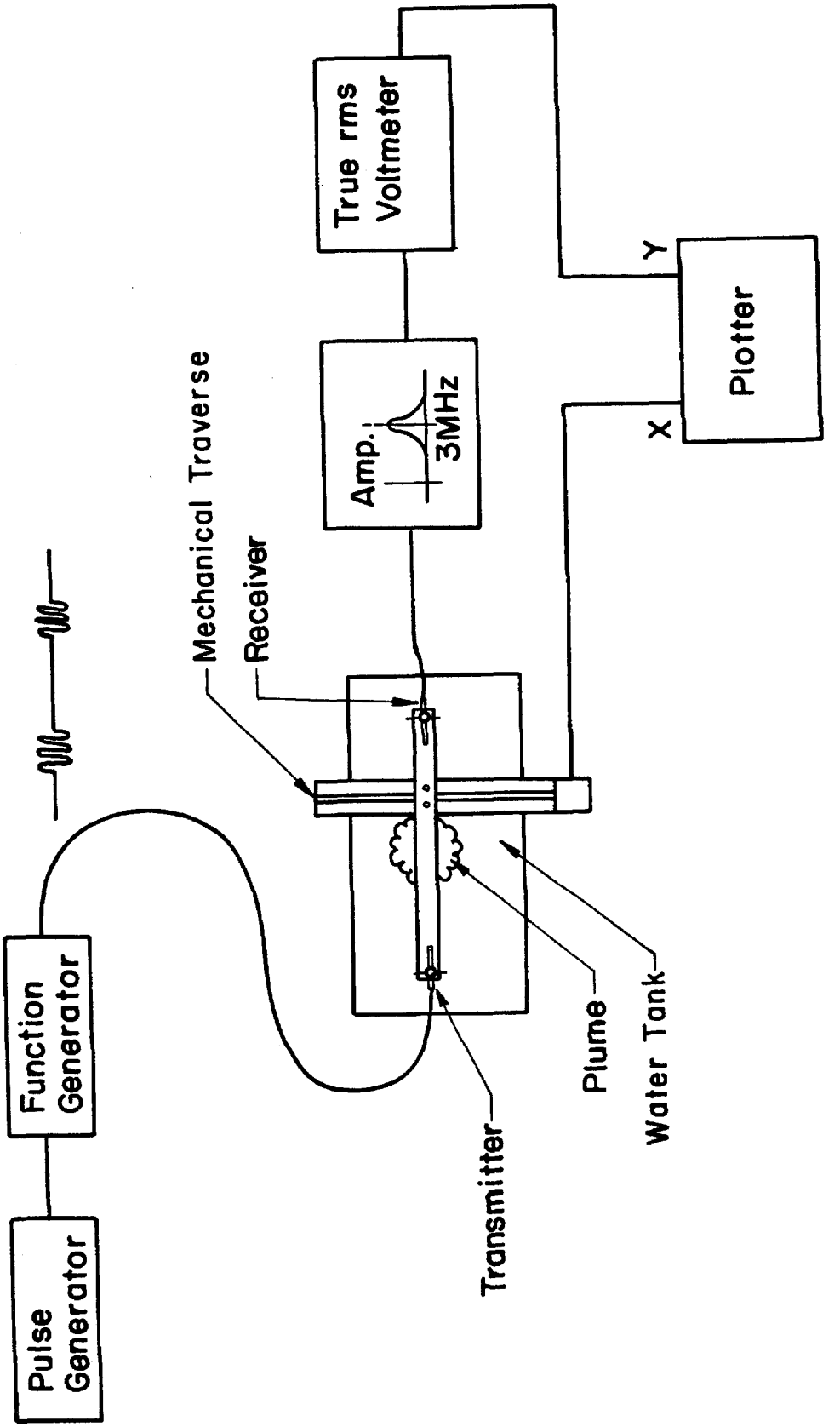

Figure E-1. Schematic of Plume Experiment

Several traces of the transmitted amplitude through the plume at a heater setting of 15 W are plotted on top of each other in Figure E-2. Since the sound speed increases with temperature, rays from the center of the plume are bent towards the edge resulting in an amplitude drop in the center and an amplitude increase near the edges of the plume. Essentially, Figure E-2 is the equivalent of a shadowgraph picture which records the ray displacement.

The temperature distribution through the center of the plume was measured with a thermocouple (iron-constantan, 0.025" diameter) and is shown in Figure E-3. Several traces are plotted on top of each other showing the repeatability of the measurements. To reconstruct the temperature profile from the sound transmission given in Figure E-2 requires the application of ray tracing techniques, which will be the subject of future studies.

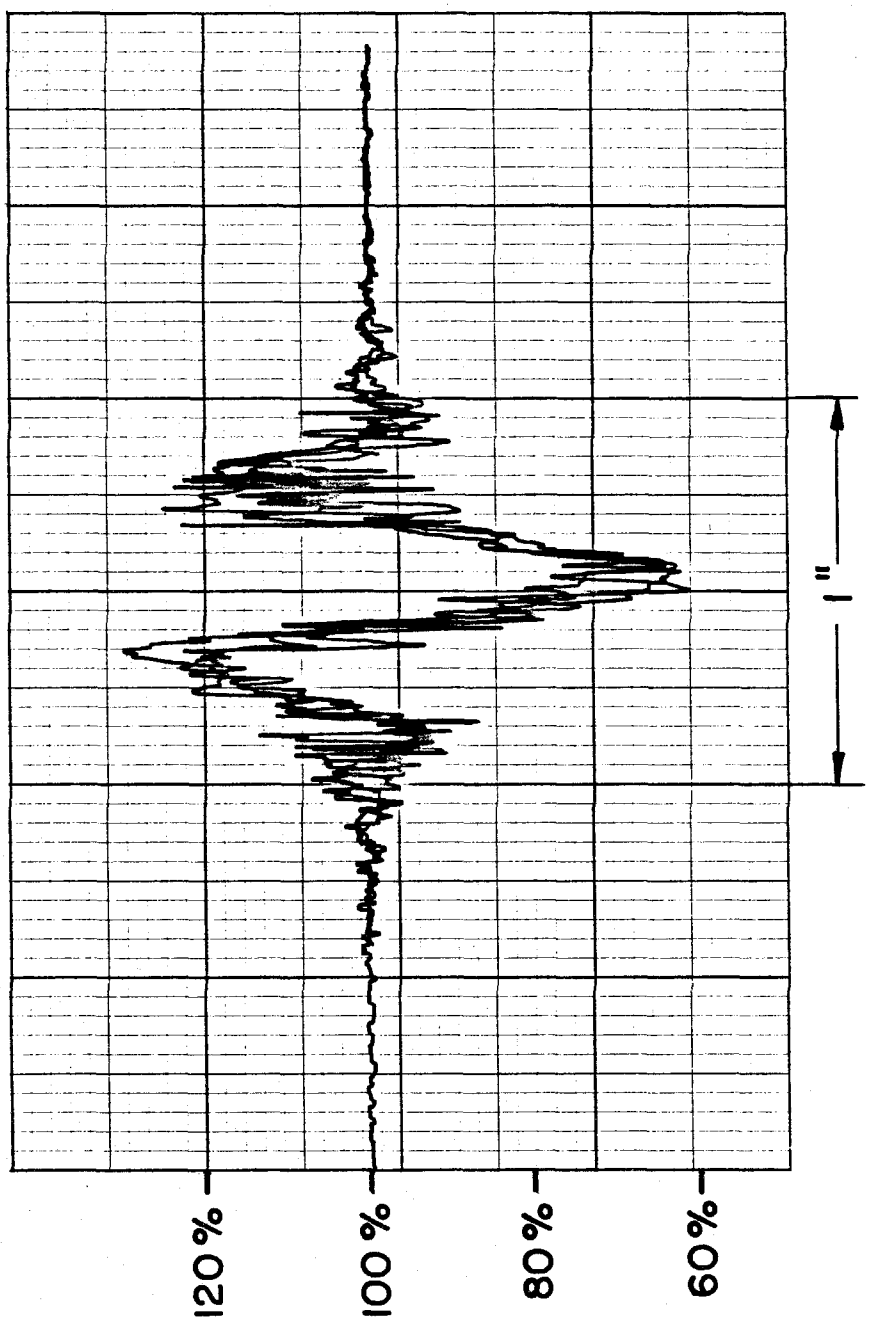

Figure E-2. Acoustic Amplitude Transmission Image of Plume at 15 W

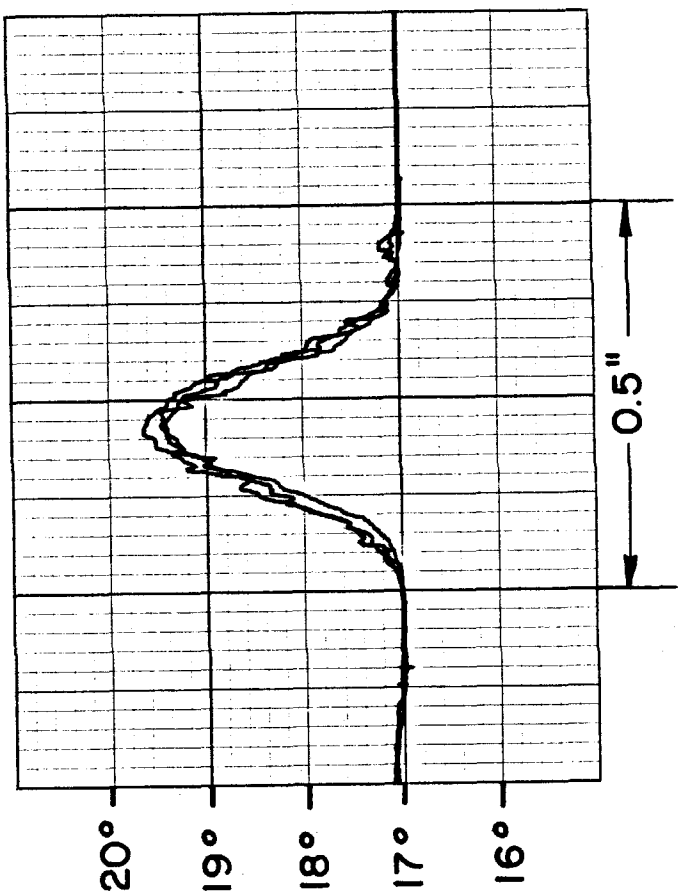

Figure E-3. Temperature Distribution through Plume at 15 W